Measurement report: Vertical and temporal variability of near-surface ozone production rate and sensitivity in an urban area in Pearl River Delta (PRD) region, China

Jun Zhou[1,2#], Chunsheng Zhang[3#], Aiming Liu[3], Bin Yuan[1,2*], Yan Wang[1,2], Wenjie Wang[1,4], Jie-Ping Zhou[1,2], Yixin Hao[1,2], Xiao-Bing Li[1,2*], Xianjun He[1,2], Xin Song[1,2], Yubin Chen[1,2], Suxia Yang[1,2], Shuchun Yang[1,2], Yanfeng Wu[1,2], Bin Jiang[1,2], Shan Huang[1,2], Junwen Liu[1,2], Yuwen Peng[1,2], Jipeng Qi[1,2], Minhui Deng[1,2], Bowen Zhong[1,2], Yibo Huangfu[1,2], Min Shao[1,2*]

[1]Institute for Environmental and Climate Research, Jinan University, Guangzhou 511443, China

[2]Guangdong-Hongkong-Macau Joint Laboratory of Collaborative Innovation for Environmental Quality, Guangzhou 511443, China

[3]Shenzhen National Climate Observatory, Shenzhen 518040, China

[4]Multiphase Chemistry Department, Max Planck Institute for Chemistry, Mainz 55128, Germany

[#]These authors contribute equally to this work.

Correspondence: Bin Yuan (byuan@jnu.edu.cn), Xiao-Bing Li (lixiaobing@jnu.edu.cn), Min Shao (mshao@jnu.edu.cn)

Abstract: Understanding the near-ground vertical and temporal photochemical O_3 formation mechanism is important to mitigate O_3 pollution. Here, we measured the vertical profiles of O_3 and its precursors at six different heights ranging from 5 to 335 m using a newly built vertical observation system in the Pearl River Delta (PRD) region, China. The net photochemical ozone production rate ($P(O_3)_{net}$) and O_3 formation sensitivities at various heights were diagnosed using an observation-based model coupled with the Master Chemical Mechanism (MCM v3.3.1). Moreover, to assess model performance and identify the causative factors behind O_3 pollution episodes, the $P(O_3)_{net}$ was measured at 5 m ground level utilizing a custom-built detection system. In total three O_3 pollution episodes and two non-episodes were captured. The identified O_3 pollution episodes were found to be jointly influenced by both photochemical

production and physical transport, with local photochemical reactions playing a major role. The high index of agreement (IOA) calculated from comparing the modelled and measured $P(O_3)_{net}$ values indicated the rationality to investigate the vertical and temporal variability of O_3 formation mechanisms using modelling results. However, the measured $P(O_3)_{net}$ values were generally higher than the modelled $P(O_3)_{net}$ values, particularly under high NOx conditions, which may indicate a potential underestimation of total RO_2 by the model. Throughout the measurement period, the contribution of different reaction pathways to O_3 production remained consistent across various heights, with HO_2+NO as the major O_3 production pathway, followed by RO_2+NO. We observed $P(O_3)_{net}$ decreasing with the increase in measurement height, primarily attributed to the decreased O_3 precursors anthropogenic volatile organic compounds (AVOC) and oxygenated volatile organic compounds (OVOC). O_3 formation regimes were similar at different heights during both episodes and non-episodes, either located in the volatile organic compounds (VOCs) sensitive regime or in the transition regime and more sensitive to VOCs. Diurnally, photochemical O_3 formation typically remained in the VOCs sensitive regime during the morning and noon, but transitioned to the transition regime and more sensitive to VOCs in the afternoon around 16:00 local time (LT). The vertical and temporal O_3 formation is most sensitive to AVOC and OVOC, suggesting that targeting VOCs, especially AVOC and OVOC, for control measures is more practical and feasible at the observation site. The vertical temporal analysis of O_3 formation mechanisms near the ground surface in this study provides critical foundational knowledge for formulating effective short-term emergency and long-term strategies to combat O_3 pollution in the PRD region of China.

1. Introduction

Tropospheric ozone (O_3), which has adverse effects on ecosystems, climate change, and human health (Fiore et al., 2009; Anenberg Susan et al., 2012; Seinfeld, 2016), has become an important factor resulting in severe regional air pollution in China (Zhu et al., 2020). Tropospheric O_3 mainly comes from stratospheric intrusions and the photochemical reactions of O_3 precursors, involving volatile organic compounds (VOCs) and nitrogen oxides ($NOx=NO+NO_2$). The O_3-precursor relationship can be split into a "NOx-limited" or "VOC-limited" or "mixed-sensitive" regime (Seinfeld and Pandis, 2016; Sillman S., 1999). A "NOx-limited" regime has higher VOCs/NOx ratios and the O_3 formation is sensitive to NOx concentration changes, while a "VOCs-limited"

64 regime has lower VOCs/NOx ratios and the O_3 formation is sensitive to VOCs
65 concentration changes. In a "mixed-sensitive" regime, O_3 formation responds
66 positively to changes in both NOx and VOC emissions (Wang et al., 2019). Local O_3
67 concentrations can be further influenced by meteorological conditions and the regional
68 transport of O_3 and its precursors (Gong and Liao, 2019; Chang et al., 2019). The Pearl
69 River Delta (PRD) stands out as one of the most rapidly developing economic and
70 urbanized regions in China, which currently is suffering from severe ground-level O_3
71 pollution (Lu et al., 2018; Yang et al., 2019). Currently, many scholars have analyzed
72 the relationship between tropospheric O_3 pollution and its precursors and
73 meteorological elements in the PRD region, results show that the surface O_3 pollution
74 is determined by both local photochemistry and physical transport, with long-range
75 transport contributing 30%-70% to surface O_3 concentrations (Mao et al., 2022; Shen
76 et al., 2021; Li et al., 2012, 2013). However, the distribution of O_3 is highly variable at
77 different altitudes (Wang et al., 2021), due to vertical differences in VOCs
78 concentrations and sources, as well as the sensitivity of O_3 formation (Liu et al., 2023;
79 Tang et al., 2017). Due to the presence of strong vertical mixing driven by the surface
80 heating effect in the daytime boundary layer, the budget of the O_3 at the ground level
81 and also at an arbitrary height in the daytime boundary layer is closely related to the
82 formation and removal of O_3 at other heights (Tang et al., 2017). In addition, the
83 difference in vertical gradients of precursors may drive the vertical change in the
84 photochemical formation regimes of O_3 (Zhao et al., 2019). Using data from only one
85 height to understand the photochemical reactions in the planetary boundary layer is of
86 great limitation. Thus, diagnosing the O_3 formation mechanism at different heights is
87 essential to achieve effective control of O_3 pollution.

88 Currently, remote sensing techniques with high time resolution and real-time
89 response, such as lidar and optical absorption spectroscopy, have been utilized to
90 measure the vertical distribution of O_3 (Luo et al., 2020a; Wang et al., 2021). However,
91 in situ measurements of VOCs at various heights primarily rely on offline methods
92 combined with diverse techniques, including aircraft, tethered balloons, tall buildings
93 and towers, unmanned aerial vehicles (UAVs or drones), and satellite observations
94 (Klein et al., 2019; Li et al., 2022; Geng et al., 2020; Benish et al., 2020; Li et al., 2021;
95 Wang et al., 2019). Owing to the low time resolution of these monitoring techniques,
96 achieving continuous vertical coverage of VOCs and NOx measurements is challenging.

97   Consequently, the vertical distribution structure of VOCs remains unclear, thus largely
98   hindering our understanding of the vertical and temporal regional O_3 formation
99   mechanism.

100   To fill the gaps in the existing studies, we utilized a newly constructed vertical
101   observation system based on the Shenzhen Meteorological Gradient Tower (SZMGT)
102   (Li et al., 2023). This system measured the vertical profiles of O_3 and its precursors at
103   six different heights from 5 to 335 m. To diagnose the net O_3 production rate, $P(O_3)_{net}$,
104   and O_3 formation sensitivities across various heights, we employed an observation-
105   based model coupled with the Master Chemical Mechanism (MCM v3.3.1), referred to
106   as OBM-MCM in the following. Additionally, we employed a novel net photochemical
107   O_3 production rate ($P(O_3)_{net}$, NPOPR) detection system to measure the $P(O_3)_{net}$ at the 5
108   m ground level to explore potential reasons for O_3 pollution episodes (Hao et al., 2023),
109   i.e., examine the contribution of chemical and physical processes to changes in O_3
110   concentration. Comparisons between the directly measured $P(O_3)_{net}$ results and the
111   model-derived data enabled us to evaluate the simulation accuracy and explore potential
112   reasons for discrepancies of the OBM-MCM model concerning photochemical O_3
113   formation. Based on these results, we have extensively discussed the vertical and
114   temporal variability in $P(O_3)_{net}$ and O_3 formation sensitivity, while acknowledging
115   potential biases associated to the modelling. The findings of this study offer a new
116   benchmark for understanding the vertical profile of photochemical O_3 formation
117   mechanism, aiding in the identification of the primary driver of ground-level O_3
118   pollution. This identification is crucial as it can provide essential theoretical support for
119   developing short-term effective emergency and long-term control measures targeting
120   O_3 in PRD region of China.

121   **2. Materials and Methods**
122   **2.1 Sampling site**

123   Field measurements were conducted at the Shenzhen Meteorological Gradient
124   Tower (SZMGT) (22.65° N,113.89° E) from November 13 to December 10, 2021. The
125   SZMGT is 365 m high and is currently the tallest mast tower in Asia and the second
126   tallest of this kind in the world. The main structure of the tower is made of steel, steel
127   stray lines are used for fixing and securing the tower. It is located in the Tiegang
128   Reservior Water Reserve at Bao'an District of Shenzhen, in the Pearl River Delta (PRD)

region of China. The area is surrounded by a high density of vegetation, reservoir features, low-rise buildings, and hills/mountains (Luo et al., 2020b).

2.2 Instrumentation

2.2.1 The vertical sampling system

A tower-based observation system for traces gases using long perfluoroalkoxy alkane (PFA) tubing (OD: 1/2") was used to sample the O_3 and O_3 precursors at six heights during the campaign, including 5, 40, 70, 120, 220, and 335 m above the ground. All six tubes were continuously drawn using a rotary vane vacuum pump to keep flushing with ambient air to reduce tube delay of the organic compounds, with the flow rate controlled by critical orifices (orifice diameter: 0.063"). A Teflon solenoid valve group was used to switch the air samples at specified time intervals so that the subsamples from these six heights could be sequentially drawn by instruments (see Fig. S1). Consequently, the flow rates of the air sample streams for the six tubes varied between 12.0 and 15.0 SLPM without subsampling and were less than 20 SLPM with subsampling. The residence time of the sample gas in the longest tube (~ 400 m) is less than 180 s at a flow rate of 13 SLPM. The impacts of long tubing on measurements of various of trace gases, including O_3, NOx, and a set of organic compounds, were systematically investigated using a combination of laboratory tests, field experiments, and modelling techniques. Field observations proved that this observation system is suitable for analyzing spatio-temporal variations of atmospheric trace gases, with many trace gases could be well measured. More details about the establishment and the characterization of this observation system are described elsewhere (Li et al., 2023).

2.2.2 $P(O_3)_{net}$ measurement

During the campaign, the $P(O_3)_{net}$ at the 5 m ground level was measured using the home-made NPOPR detection system, which was built based on the dual-channel reaction chambers technique. The improvement, characterization, and the photochemical O_3 formation mechanism in the reaction and reference chambers of the NPOPR detection system are described in our previous study (Hao et al., 2023). Briefly, the NPOPR detection system consists of reaction and reference chambers with the same geometry and made of quartz glass. The length and inner diameter of the quartz glass cylinder are 700 mm and 190.5 mm, respectively, which resulted in an inner volume of ~ 20 L. The outer surface of the reference chamber was covered with an Ultem film

161 (SH2CLAR, 3 M, Japan) for ultraviolet (UV) protection, which can block sunlight with

162 wavelengths < 390 nm, thus preventing photochemical reactions inside. During the

163 experiment, both the reaction and reference chambers were placed outdoors and directly

164 exposed to sunlight to simulate real ambient photochemical reactions. Ambient air was

165 introduced into the reaction and reference chambers at the same flow rate, and a Teflon

166 filter was mounted before the chamber inlet to remove fine particles. To correct for the

167 effect of fresh NO titration to O_3, we use O_X (=O_3+NO_2) instead of O_3 to quantify the

168 O_3 generated by photochemical reactions (Pan et al., 2015; Tan et al., 2018). A stream

169 of air from the two chambers was alternately introduced into an NO-reaction chamber

170 every 2 min to convert O_3 in the air to NO_2 in the presence of high concentrations of

171 NO (O_3+NO→NO_2), and the Ox concentrations from the outlet NO-reaction chamber,

172 i.e., the total NO_2 concentrations including the inherent NO_2 in the ambient and that

173 converted from O_3, were measured by a Cavity Attenuated Phase Shift (CAPS) NO_2

174 Monitor (Aerodyne research, Inc., Billerica MA, USA) to avoid other nitrogen oxide

175 interferences to the NO_2 measurement (such as alkyl nitrates, peroxyacyl nitrates,

176 peroxynitric acid, nitrogen pentoxide, etc.). $P(O_3)_{net}$ was obtained by dividing the

177 difference between the Ox concentrations in the reaction and reference chambers (ΔOx)

178 by the mean residence time of air in the reaction chamber $\langle \tau \rangle$:

179 $$P(O_3)_{net} = P(O_X)_{net} = \frac{\Delta O_x}{\tau} = \frac{[O_x]_{reaction} - [O_x]_{reference}}{\tau} \qquad (1)$$

180 A schematic of the NPOPR detection system is shown in Fig. S2. The pulse

181 experiments were performed to quantify the residence time in the chambers (Hao et al.,

182 2023).

183 [Ox] values plugged in Eq. (1) to derive $P(O_3)_{net}$ are measured values corrected

184 for wall losses of Ox and the light-enhanced loss of O_3 ($d[O_3]$) in the reaction and

185 reference chambers during daytime (Hao et al., 2013):

186 $$\gamma = \frac{d[O_3] \times D}{\omega \times [O_3] \times \tau} \qquad (2)$$

187 where γ is the light-enhanced loss coefficient of O_3, which is derived from $J(O^1D)$

188 according to the relationship obtained from the outdoor experiments (for more details,

189 see supplementary materials: Sect. S3). $d[O_3]$ represents the difference between the O_3

190 mixing ratios at the inlet and outlet of the reaction and reference chambers, D is the

191   diameter of the chambers, ω is the average velocity of O$_3$ molecules, [O$_3$] is the injected

192   O$_3$ mixing ratio at the inlet of the reaction and reference chambers, and τ is the average

193   residence time of the air in the reaction and reference chambers. When quantifying the

194   light-enhanced O$_3$ loss (d[O$_3$]) during the ambient air measurement, we first calculate

195   γ using the measured J(O^{1}D) and the γ -J(O^{1}D) equations listed in Fig. S8 in the

196   reaction and reference chambers, then use the measured [O$_3$] and Eq. (2) to calculate

197   d[O$_3$]. The results show that such kind of correction can increase the measured P(O$_3$)$_{net}$

198   by 10% (25% percentile) to 24% (75% percentile), with a median of 17%.

199   The limit of detection (LOD) of the NPOPR detection system is 2.3 ppbv h^{-1} at the

200   sampling air flow rate of 5 L min^{-1}, which is obtained as three times the measurement error of

201   P(O$_3$)$_{net}$ (Hao et al., 2013). The measurement error of P(O$_3$)$_{net}$ is determined by the estimation

202   error of Ox in the reaction and reference chambers, which includes the measurement error

203   associated with the O$_X$ of the CAPS-NO$_2$ monitor and the error due to the light-enhanced loss

204   of O$_3$. This collective measurement error is referred to as the measurement precision of the

205   NPOPR detection system, with further details provided in the supplementary materials,

206   specifically in Sect. S4. The measurement accuracy of the NPOPR detection system is

207   determined as 13.9 %, representing the maximum systematic error resulting from

208   photochemical O$_3$ production in the reference chamber. Our earlier research indicated that the

209   modelled P(O$_3$)$_{net}$ in the reaction chamber is similar to that modelled in ambient air, with the

210   modelled P(O$_3$)$_{net}$ in the reference chamber accounting for 0-13.9% of that in the reaction

211   chamber (Hao et al., 2023). This is due to the UV protection Ultem film covered on the

212   reference chamber, which only filtered out the sunlight with wavelengths < 390 nm, allowing

213   photochemical O$_3$ production persist at the sunlight wavelength between 390 nm and 790 nm.

214   Here, we have utilized the same modelling approach described in Hao et al. (2013) to quantify

215   the P(O$_3$)$_{net}$ in the reference chamber and corrected for the bias introduced by the measurement

216   accuracy.

2.2.3 VOCs measurement

218   VOCs were measured using a high-resolution proton transfer reaction time-of-

219   flight mass spectrometer (PTR-TOF-MS, Ionicon Analytik, Austria) (Wang et al.,

220   2020a; Wu et al., 2020) and an off-line gas chromatography mass spectrometry flame

221   ionization detector (GC-MS-FID) (Wuhan Tianlong, Co. Ltd, China) (Yuan et al.,

222   2012). The concentrations of oxygenated VOCs (OVOC), including formaldehyde

223   (HCHO) and acetaldehyde (CH$_3$CHO), were measured via PTR-TOF-MS, and the non-

224   methane hydrocarbons (NMHC) were measured via GC-MS-FID. PTR-TOF-MS was

225 run with both hydronium ion (H_3O^+) (Yuan et al., 2017; Wu et al., 2020) and nitric

226 oxide ion (NO^+) (Wang et al., 2020) modes. The measurement error of PTR-TOF-MS

227 was lower than 20%, more details of the PTR-TOF-MS technique can be found in our

228 previous publication (Yuan et al., 2017). The H_3O^+ and NO^+ modes were automatically

229 switched with 20 min H_3O^+ mode and 10 min NO^+ mode. The background signal of

230 each mode was measured every 30 min for at last 2 min by automatically switching the

231 ambient measurement to a custom-built platinum catalytic converter heated to 365 °C.

232 Operating the PTR-ToF-MS instrument in NO^+ mode primarily detects higher alkanes,

233 which are known significantly contribute to the formation of secondary organic aerosols

234 (SOA) but negligible contributions to photochemical O_3 formation (Wang et al., 2020).

235 Eventually, we only used VOCs measured during the H_3O^+ mode, which was operated

236 at a drift tube pressure of 3.8 mbar, a temperature of 120 °C, and a voltage of 760 V,

237 resulting in an E/N (E refers to the electric field and N refers to the number density of

238 the buffer gas in the drift tube) value of ~ 120 Td (townsend). 3035 ions with m/z up to

239 510 were obtained at time resolutions of 10 s. A gas standard with 35 VOC species was

240 used for calibrations of the PTR-ToF-MS once per day. Raw data from PTR-TOF-MS

241 were analyzed using Tofware software (Tofwerk AG, v3.0.3). Due to the humidity

242 dependencies of various VOCs signals of the PTR-ToF-MS observed in laboratory

243 studies, such as formaldehyde, benzene, methanol, ethanol, and furan (Wu et al., 2020),

244 we determined their humidity-dependence curves. During data analysis, we removed

245 the impacts of ambient humidity change on the measured signals of the PTR-ToF-MS

246 according to these humidity-dependence curves. For the off-line GC-MS-FID

247 measurement, whole-air samples were collected using 3.2 L electro-polished stainless-

248 steel canisters (Entech, USA) at 5 and 120 m at time intervals of two hours. Two

249 automatic canister samplers connected to 12 canisters were used to collect the whole-

250 air samples, with each of canister collecting the sample for 10 min. The canisters were

251 analyzed within one week (Zhu et al., 2018). The concentrations of 56 NMHC species

252 in the canister analyzed by GC-MS/FID were calibrated daily using the mixture of a

253 photochemical assessment monitoring stations (PAMS) standard gas and pure N_2. In

254 addition, the mixture of PAMS standard gas and pure N_2 with species concentrations

255 of 1 ppbv was injected into the analytical system every 10 samples to check the

256 operational stability of the instrument. Pure N_2 was injected into the analytical system

257 at the start and end of each day's analysis to provide reference blank measurements. A

258 full list of all 56 non-methane hydrocarbons (NMHCs) can be found in the

259   supplementary material (Table S2).

2.2.4   Other parameters

261   The photolysis frequencies of different species were measured using the actinic

262   flux spectrometer (PFS-100, Focused Photonics Inc, China). O_3, CO, and NO_X

263   concentrations were measured by a 2B O_3 monitor based on dual-channel UV-

264   absorption (Model 205, 2B Technologies, USA), a gas filter correlation (GFC) CO

265   analyzer (Model 48i, Thermo Fisher Scientific, USA), and a chemiluminescence NOx

266   monitor (Model 42i, Thermo Fisher Scientific, USA), respectively. According to our

267   test (Zhou et al., 2025), a 5% overestimation could be caused in the NO_2 measurement

268   using the chemiluminescence technique compared to the CAPS technique, due to some

269   NO_Z species (i.e., HNO_3, peroxyacetyl nitrate (PANs), HONO, etc.)(Dunlea et al.,

270   2007), this will result in a decrease of the modelled $P(O_3)_{net}$ by < 4%, which is

271   negligible compared to the bias caused by the $P(O_3)_{net}$ in the reference chamber (~ 14%)

272   (Zhou et al., 2023).Temperature (T), relative humidity (RH), and pressure (P) were

273   measured by a portable weather station (Met Pak, Gill Instruments Ltd, UK).

2.3 Data analysis

2.3.1   Observation-based chemical box model

276   We investigated the detailed photochemical O_3 formation mechanism during the

277   observation period based on the field observed data. The specific tropospheric O_3

278   photochemical formation process involves the photolysis of NO_2 at < 420 nm

279   (Sadanaga et al., 2017). Simultaneously, RO_X (RO_X=OH+HO_2 +RO_2) radical recycles

280   provide HO_2 and RO_2 to oxidize NO to NO_2, resulting in the accumulation of O_3 (Shen

281   et al., 2021; Cazorla and Brune, 2010; Sadanaga et al., 2017). Therefore, the ROx

282   radicals and the O_3, OH, NO_3 oxidants play important roles in photochemical O_3

283   formation. A zero-dimensional box model based on the Framework for 0-D

284   Atmospheric Modelling (F0AM) v3.2 (Wolfe et al., 2016) coupled with the MCM

285   v3.3.1 was used to simulate the $P(O_3)_{net}$. MCM v3.1.1 contains a total of 143 VOCs,

286   more than 6700 species, involving more than 17000 reactions (Jenkin et al., 2015).

287    $P(O_3)_{net}$ and O_3 concentrations were simulated by constraining T, RH, P, organic and

288   inorganic substances in gases, including 12 OVOCs (methanol, ethanol, formaldehyde,

289   acetaldehyde, acrolein, acetone, hydroxyacetone, phenol, m-cresol, methyl vinyl ketone,

290   methacrylaldehyde, methyl ethyl ketone), 56 NMHCs (toluene, benzene, isoprene,

styrene, etc. as listed in Table S2), inorganic gaseous pollutants (O_3, NO, NO_2, and CO), and photolysis rate values ($J(O^1D)$, $J(NO_2)$, $J(H_2O_2)$, $J(HONO)$, $J(HCHO\_M)$, $J(HCHO\_R)$, $J(NO_3\_M)$, $J(NO_3\_R)$, etc.). The VOCs, NOx, T, RH and P were constrained throughout the modelling period, while O_3 was not constrained after providing initial concentration values. To avoid the build-up of long-lived species to unreasonable levels, we also considered the physical dilution process by setting a constant dilution factor of 1/43200 s^{-1} throughout the modelling period (Liu et al., 2021; Decker et al., 2019). Additionally, the dry deposition rate of O_3 was set to 0.42 cm s^{-1}, and the background of O_3, CO, and CH_4 were set to 30, 70, and 1800 ppbv, respectively, based on the findings of Wang et al. (2011), Wang et al. (2022a), and WMO greenhouse gas bulletin (2022). The modelling was run in a time-dependent mode with a resolution of 5 min, and it was run for spin-up time of 72 h to establish steady-state concentrations for secondary pollutants that were not constrained during the simulation. $P(O_3)_{net}$ can be expressed by the difference between O_3 production rate ($P(O_3)$) and O_3 destruction rate ($D(O_3)$), where $P(O_3)$ and $D(O_3)$ can be calculated as Eq. (3)-(4):

$$P(O_3) = k_{HO_2+NO}[HO_2][NO] + \sum_i k_{RO_{2,i}+NO}[RO_{2i}][NO]\varphi_i \tag{3}$$

$$D(O_3) = k_{O(^1D)+H_2O}[O(^1D)][H_2O] + k_{OH+O_3}[OH][O_3] + k_{HO_2+O_3}[HO_2][O_3]$$

$$+ k_{O_3+alkenes}[O_3][alkenes] + k_{OH+NO_2}[OH][NO_2] +$$

$$k_{RO_{2,i}+NO_2}[RO_{2i}][NO_2] \tag{4}$$

where k_{M+N} represents the bimolecular reaction rate constant of M and N, the subscript 'i' refers to different types of RO_2, and φ_i is the yield of NO_2 of the reaction RO_{2i}+NO. The relevant reaction rates of $P(O_3)$ and $D(O_3)$ and the mean measured concentrations of each VOC category at 5 m ground during O_3 episodes and non-episodes used in the model are listed in Tables S1 and S2.

2.3.2 Derive contribution of chemical and physical processes to O3 changes on the ground level

It is known that chemical and physical processes jointly influence the O_3 concentration changes near the ground surface (Xue et al., 2014; Tan et al., 2019). The direct measurement of $P(O_3)_{net}$ gave us a chance to identify the contribution of chemical and physical processes to the variation of observed O_3 concentrations using the following equation:

$$\frac{dO_X}{dt} = P(O_X)_{net} + R(O_X)_{trans} \tag{5}$$

Where $\frac{dO_X}{dt}$ is the change rate of the observed O_x mixing ratio change (ppbv h^{-1}), $P(Ox)_{net}$ denotes the net photochemical O_3 production rate (ppbv h^{-1}), which was equal to $P(O_3)_{net}$ and measured directly by the NPOPR system. $R(O_X)_{trans}$ represents O_3 mixing ratio change due to physical transportation (ppbv h^{-1}), including the horizontal and vertical transport, dry deposition and the atmospheric mixing (Liu et al., 2022). To correct the effects of NO titration to O_3, we have replaced O_3 with O_X (=O_3+NO_2) during the calculation in this study (Pan et al., 2015).

2.3.3 Model performance

In order to judge the reliability of the model simulation, we calculated the index of agreement (IOA) based on the measured and modelled $P(O_3)_{net}$ and O_3 at 5 m above the ground level using the following equation (Liu et al., 2019):

$$IOA = 1 - \frac{\sum_{i=1}^{n}(O_i - S_i)^2}{\sum_{i=1}^{n}(|O_i - \bar{O}| - |S_i - \bar{O}|)^2} \tag{6}$$

Where S_i and O_i represents the simulated and observed $P(O_3)_{net}$ or O_3 values at the same time, respectively, $\bar{O}$ is the averaged observed value, and n is the data number. Furthermore, we also judged the model simulation performance using statistical measures, including the normalized mean bias (NMB) and normalized mean error (NME), which are defined as:

$$NMB = \frac{\sum_{i=1}^{n}(S_i - O_i)}{\sum_{i=1}^{n} O_i} \cdot 100\% \tag{7}$$

$$NME = \frac{\sum_{i=1}^{n}|S_i - O_i|}{\sum_{i=1}^{n} O_i} \cdot 100\% \tag{8}$$

Where S_i and O_i have the same meaning as Eq. (6), and n is the total number of such data pairs of interest. The results will be discussed in Sect. 3.2.2.

2.3.4 OH reactivity

In order to investigate the influence of the photochemical reactions of different VOCs to photochemical O_3 formation, we calculated the OH reactivities of different VOCs, which is the sum of concentrations of OH reactants multiplied by their reaction rate coefficients, as shown below:

$$k_{OH} = k_i \times [VOCs]_i \qquad (9)$$

where k_{OH} represents the total OH reactivity of a group of VOCs species, k_i represents the rate constants between OH radicals and different VOCs species i, $[VOCs]_i$ represents the concentration of species i. In this study, we summarized the OH reactivities of different kinds of VOCs groups together to investigate their influence on the vertical gradient $P(O_3)_{net}$ in Sect. 3.2.3.

2.3.5   O$_3$ formation potential

The O$_3$ formation potential is calculated using the product of the VOCs concentration and the maximum incremental reactivity (MIR) coefficient (dimensionless, gram of O$_3$ produced per gram of VOCs) (Carter et al., 2012):

$$OFP_i = \sum_i [VOC]_i \times MIR_i \qquad (10)$$

Where OFP$_i$ is the O$_3$ formation potential of species i, $[VOC]_i$ is the mass concentration or emission of species i, and MIR$_i$ denotes the maximum increment reactivity of species i (g O$_3$/g VOCs).

2.3.6   O$_3$ formation regime

The sensitivity of photochemical O$_3$ production to its precursors was diagnosed by calculating the relative incremental reactivity (RIR) using the OBM-MCM model. RIR is defined as the percent change in O$_3$ photochemical production per percent change in the concentration of its single precursor/precursor group (Cardelino and Chameides, 1995). Therefore, the RIR for precursor (group) X can be expressed as:

$$RIR = \frac{\Delta P(O_3)/P(O_3)}{\Delta X/X} \qquad (11)$$

where the $\Delta X/X$ represent the percent change in different O$_3$ precursors or precursor groups. We classified the measured VOCs into anthropogenic organic compounds (AVOC), biogenic organic compounds (BVOC), and OVOC group, and investigated the O$_3$ formation sensitivity to these different types of VOCs.

3.   Results and discussions

3.1 Vertical and temporal profile of O$_3$ and its precursors

3.1.1 O$_3$ and its precursors at 5 m ground level

Figure 1 shows the time series of the major trace gases, photolysis rate constants,

and meteorological parameters at 5 m ground-level during the observation period at SZMGT. Over the 1-month field observation period, a total of 3 O_3 pollution episodes (referred to episodes hereafter) and 2 non-O_3 pollution episodes (referred to non-episodes hereafter) were captured. O_3 pollution episodes were defined as the days during which the hourly average O_3 concentration at ground-level (5 m) exceed the Grade II standard (102 ppbv, GB 3095-2012, China; Ambient Air Quality Standards, 2012), while the remaining days were defined as non-episodes. Episode days (marked as gray columns in Fig. 1) included November 13-18 (episode I), November 26 (episode II), and December 7-9 (episode III), while the non-episode days included November 22-25 (non-episode I), November 26-27 and 30 (non-episode II). The corresponding daytime mean values (6:00-18:00 LT) during all episode days and non-episode days are shown in Table 1. During the daytime of episode days (episodes I, II, and III), the mean concentrations of O_3 were 70.1±28.6, 59.5±32.4, and 71.3±31.0, respectively. The mean T and RH were 22.3±2.5 °C and 56.2±14.5 % for episode I, 20.4±3.2 °C and 52.2±16.7 % for episode II, and 20.6±3.4 °C and 58.2±17.2 % for episode III. During non-episode days, the mean concentrations of O_3 were 45.3±16.2 and 63.7±21.3 ppbv for non-episode I and II, respectively. The corresponding mean T and RH were 18.4±4.3 °C and 69.5±15.4 % for non-episode I, and 21.3±2.7 °C and 51.8 ±13.7 % for non-episode II. These observations indicate that the T and RH during episode days were not significantly different from those during non-episode days. This phenomenon contrasts with previous studies in the PRD area, where O_3 pollution episodes were generally associated with high T and low RH (Mousavinezhad et al., 2021; Hong et al., 2022).
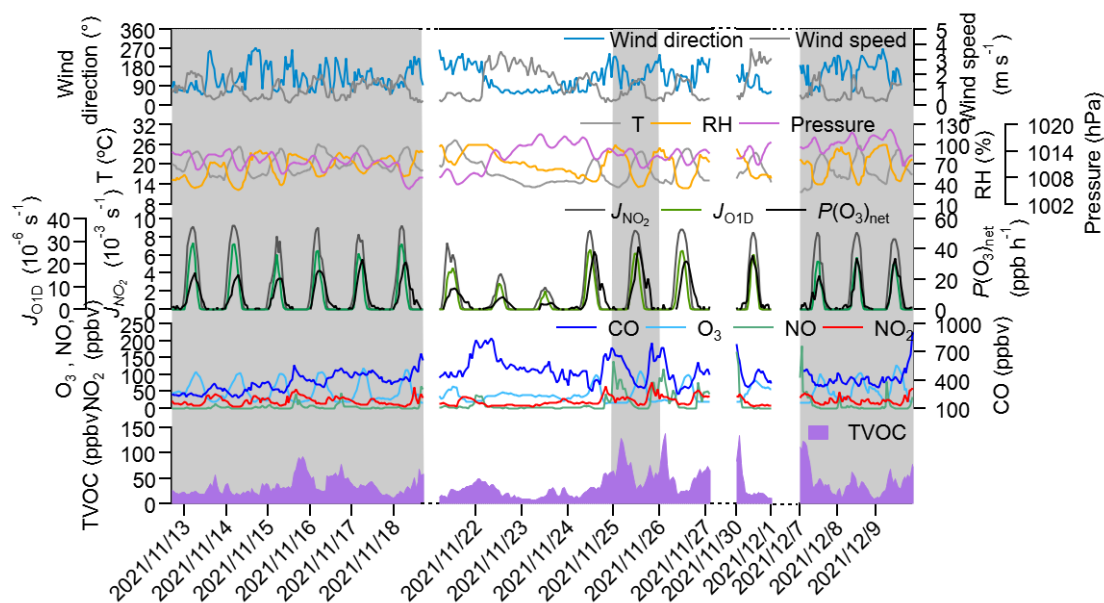
401

402 **Figure 1. Time series of major trace gases, photolysis rate constants, and meteorological**

403 **parameters at 5 m ground level during the observation period. The gray columns show the**

404 **typical O_3 episodes that occurred.**

405 **Table 1. Daytime major trace gases concentrations (units: ppbv), $P(O_3)_{net}$ (units: ppbv h**
406 **[-1]), and meteorological parameters during different episodes and non-episodes during the**
407 **observation period (from 13 November to 9 December 2021) at SZMGT.**

Parameters	Mean±SD				
	Episode I	Episode II	Episode III	Non-episode I	Non-episode II
O_3	70.1±28.6	59.5±32.4	71.3±31.0	45.3±16.2	63.7±21.3
TVOC	29.6±10.6	53.8±21.7	42.9±11.5	23.3±8.6	26.8±11.1
CO	344.9±85.1	408.8±85.4	397.2±42.1	508.5±117.2	383.4±74.6
NO	2.3±2.6	13.1±17.4	6.6±13.8	2.9±2.0	6.8±13.1
NO_2	15.6±7.5	22.3±10.2	20.0±8.3	14.1±6.8	15.4±8.8
OFP (g m^{-3})	5.1E-4± 7.5E-5	1.0E-3± 2.0E-4	7.2E-4± 8.3E-5	4.1E-4± 5.6E-5	4.7E-4± 7.8E-5
$P(O_3)_{net}$* ppbv h^{-1})	14.3±10.7	21.5±14.9	14.6±11.9	5.6±4.6	18.9±13.9
T (℃)	22.3±2.5	20.4±3.2	20.6±3.4	18.4±4.3	21.3±2.7
RH (%)	56.2±14.5	52.2±16.7	58.2±17.2	69.5±15.4	51.8±13.7
Wind speed (m s^{-1})	1.3±0.5	1.2±0.4	1.1±0.5	1.8±0.9	2.1±0.9
wind direction (°)	115.5±48.7	128.6±35.3	144.8±57.1	115.0±57.6	115.3±36.2

408 * All values here were calculated as the mean average values during daytime (6:00-18:00 LT).

409 The mean concentrations of O_3 precursors, including CO, NO, NO_2, and the total

VOCs measured by PTR-TOF-MS (shown as TVOC in Fig. 1 and Table 1), did not exhibit notable discrepancies between episodes and non-episodes. This suggests that their concentrations during O_3 pollution episodes can vary, being either higher or lower than those observed during non-episodes (as shown in Table 1). For example, through there are days with very high hourly average O_3 concentrations which define O_3 pollution episodes-where levels exceed the Grade II standard of 102 ppbv-the overall average O_3 concentrations for episode II is not higher than that of non-episode II. This suggests that despite the occurrence of peak hourly levels, the average concentration for episode II remains lower, highlighting the fluctuating pattern of O_3 levels during these episodes. Further comparison of the daytime mean O_3 formation potential (OFP) and the measured $P(O_3)_{net}$ during episodes and non-episodes showed no significant differences, ranging from 5.1×10^{-4} to 1.0×10^{-3} g m^{-3} and 14.3 to 21.5 ppb h^{-1}, respectively, during non-episodes, whereas they are ranged from 4.1×10^{-4} to 4.7×10^{-4} g m^{-3} and 5.6 to 18.9 ppb h^{-1} respectively, during episodes. Although OFP was always higher during episodes than during non-episodes, the mean $P(O_3)_{net}$ values during episodes I and III were even lower than during non-episodes II. The higher O_3 concentrations may be due to the more stable weather conditions during episodes I and III (with lower wind speed), which benefits the accumulation of O_3 formed by local photochemical O_3 formation. While for non-episode II, even it processes higher $P(O_3)_{net,}$ the outflow of O_3 from the observation site by physical processes may be higher due to the higher wind speed. These findings indicate that the O_3 pollution episodes stem from either substantially elevated local photochemical O_3 formation (i.e., episode II), or the accumulation of O_3 formed by moderate local photochemical O_3 formation under stable weather conditions (i.e., episodes I and II). Notably, when local photochemical reactions contribute intensely to the formation of O_3, favorable weather conditions facilitating O_3 outflow diminish the likelihood of O_3 pollution occurrences (i.e., non-episode II). These results indicate that O_3 pollution episodes are jointly affected by the photochemical reactions and physical transport processes, which we will discuss in more detail in Sect. 3.2.1.

440
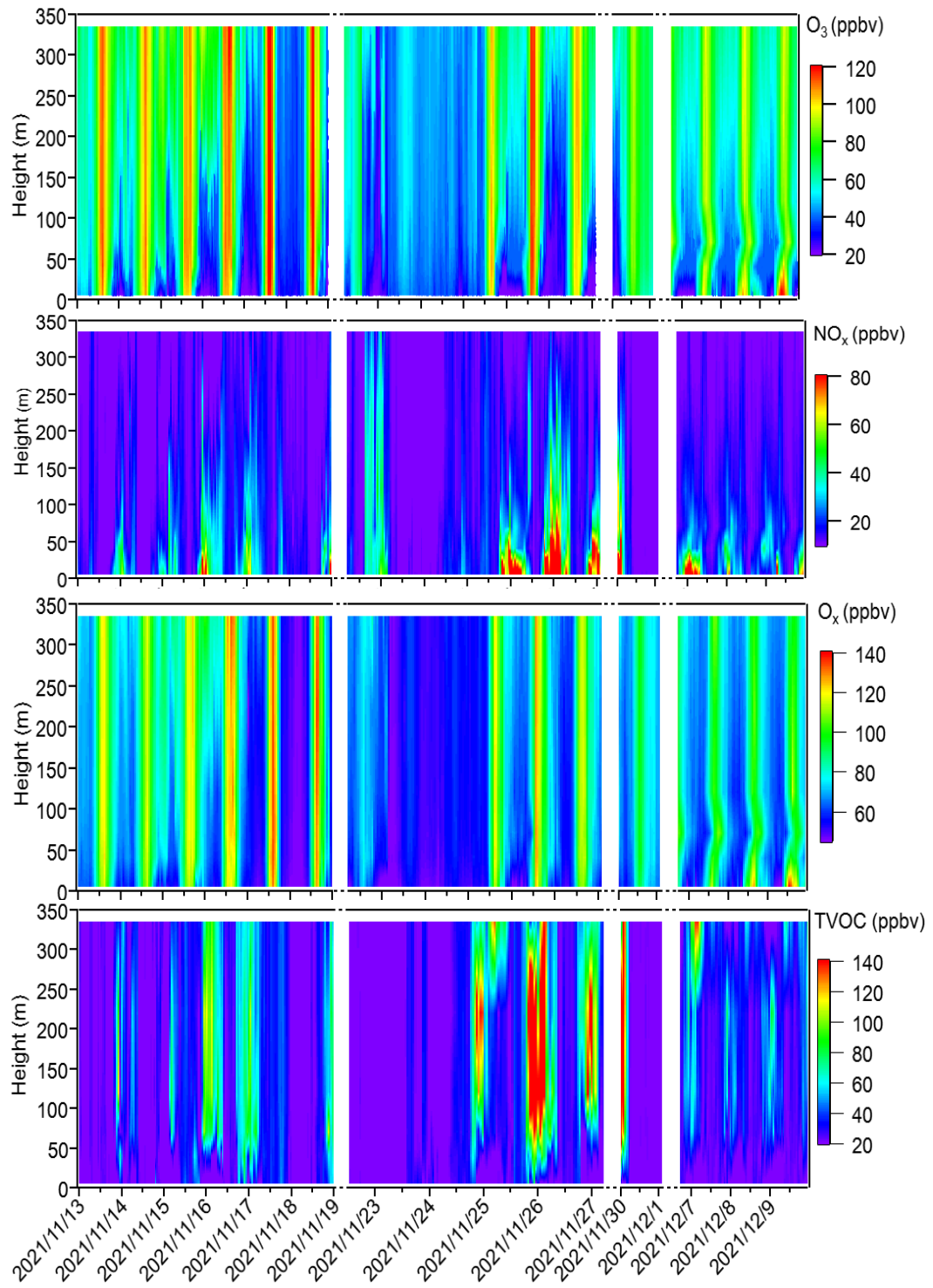
Figure 2. Time series of vertical profiles for O₃, NOx, Ox, and TVOC during the observation period. The contour plots are made using the measured values from six heights.

443
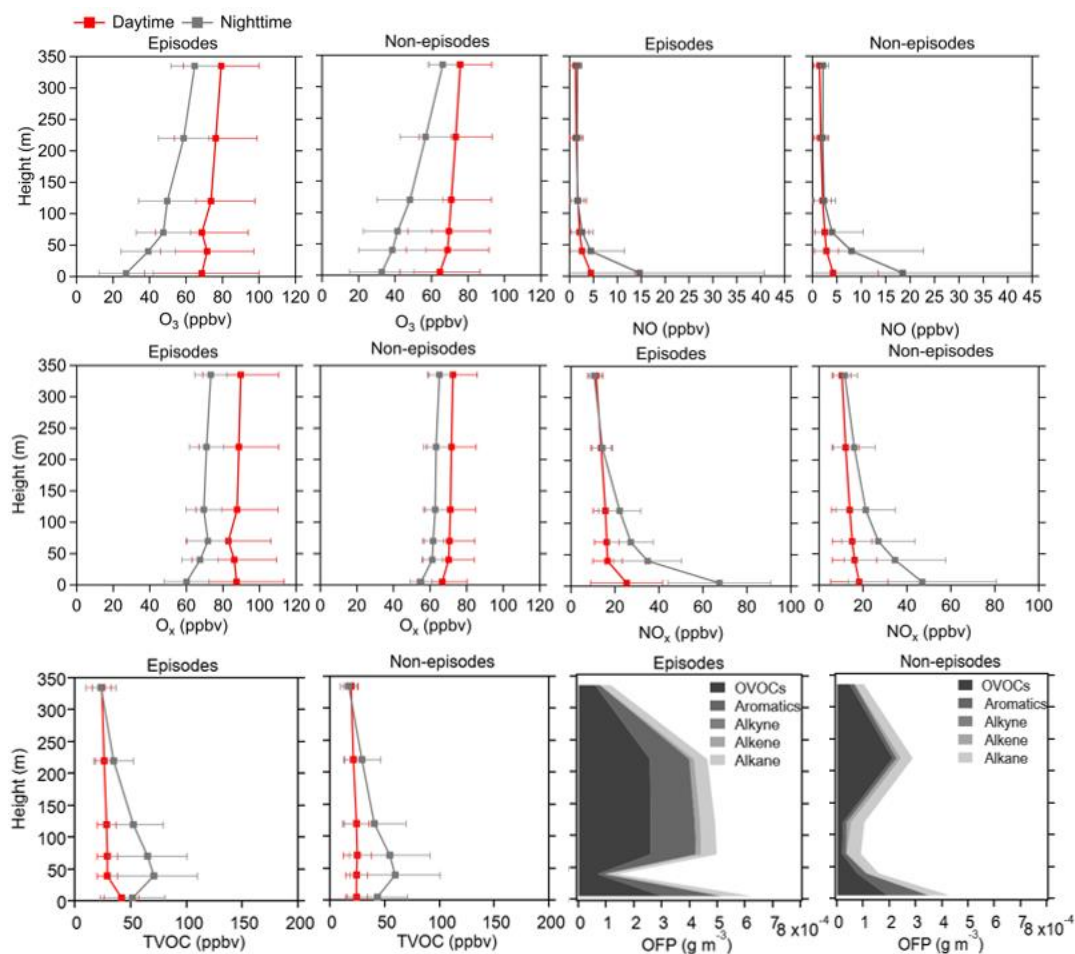
Figure 3. Average vertical profiles of O_3, NO, Ox, NOx, and TVOC during both daytime and nighttime, and OFP of different VOCs types during daytime at six heights (5, 40, 70, 120, 220, and 335 m), including episodes and non-episodes throughout the observation period. The error bars indicate the standard deviation calculated from the measured values during these periods.

3.1.2 Vertical profiles of O_3 and its precursors at 5-335 m level

Figure 2 shows the contour plots illustrating the vertical profiles of O_3, NOx, Ox(=O_3+NO_2), and TVOC. From Fig. 2, minimal vertical gradients were observed during daytime in the concentration of all species–O_3, NOx, Ox, and TVOC–due to the rapid vertical mixing effects. However, distinct vertical gradients were observed during nighttime owing to the stability of the nocturnal residual layer. Elevated concentrations of O_3 and Ox were identified at higher altitudes, whereas higher NOx concentrations predominantly occurred at ground level. We further elucidated the vertical distribution patterns of different pollutants as well as the OFP of different VOCs groups during local daytime (6:00-18:00 LT) and nighttime (19:00-5:00 LT) for both episodes and non-episodes, as shown in Fig. 3.

461  The vertical profiles of averaged concentrations of various pollutants exhibit
462 similar trends during both episodes and non-episodes, with O_3 showing an increasing
463 trend from 5 m above ground level to 355 m, aligning with findings from previous
464 studies (Zhang et al., 2019; Wang et al., 2021). Given that NOx has a significant
465 titration effect on O_3, the lower O_3 concentration at ground level may be attributed to
466 the increase in NOx concentration (Zhang et al., 2022) and also the dry deposition near
467 the ground (Li et al., 2022). NO and NOx showed an opposite trend compared to O_3.
468 These two factors jointly effected the Ox changing trend with heights, and consequently,
469 the gradients of Ox concentrations showed a weaker increasing trend from the 5 m
470 ground level to 355 m height compared to O_3. This observation demonstrated a more
471 pronounced NO titration effect at the 5 m ground level compared to the effect at 355 m
472 height. However, the TVOC showed variable trends with increased height for daytime
473 and nighttime during episodes and non-episodes. During daytime, TVOC initially
474 decreased from 5 m to 40 m, and then continuously increased from 40 m to 355 m
475 during episodes, while continuously slightly decreased from 5 m to 335 m during non-
476 episodes. During nighttime, TVOC concentrations first increased from 5 m to 40 m and
477 then continuously decreased from 40 m to 335 m during both episodes and non-episodes.
478 We further plotted the OFP of different VOCs groups at various altitudes, and found
479 that the total OFP was highest at 5 m ground level and exhibited higher levels during
480 episodes compared to non-episode periods. Subsequently, there was a significant
481 decrease at 40 m height during both episodes and non-episodes. However, there was a
482 sharp increase observed at 70 m, 120 m, and 220 m during episodes, contrasting with a
483 gradual rise during non-episode periods, which eventually reach a peak at 220 m during
484 non-episodes. A consistent decrease of OFP from 220 m to 335 m was observed during
485 both episodes and non-episodes. The OFP was primarily attributed to OVOCs at
486 different altitudes throughout both episodes and non-episodes, followed by aromatics
487 and alkane during episodes and non-episodes, respectively.

488  In conclusion, our daytime observations revealed minimal vertical gradients in the
489 concentrations of O_3, NOx, Ox, and TVOC, attributed to the rapid vertical mixing
490 effects driven by surface heating effects (Tang et al., 2017). This suggests that ground-
491 level O_3 concentrations would be representative of the entire vertical column.
492 Nonetheless, the OFP varies for different VOCs profiles at various heights, and the
493 vertical mixing effects facilitates the downward transport of O_3 photochemically

formed from higher altitudes to the near-ground layer. Consequently, a box model constraining to ground-level NOx and VOCs concentrations may not accurately reflect the in situ O_3 production in the vertical atmospheric column.

3.2 O_3 pollution episodes formation mechanism at near-ground surface

In this section, we first explored the possible reason for O_3 pollution episodes on the 5 m ground level, aiming to identify the contribution of chemical and physical processes to change in O_3 concentrations (Sect. 3.2.1). Subsequently, we assessed the modelling performance and investigated the potential reasons for the modelling bias in photochemical O_3 formation by comparing the measured $P(O_3)_{net}$ with the modelled $P(O_3)_{net}$ (Sect. 3.2.2). To gain insights into the photochemical O_3 formation mechanism at different heights and understand their role in overall O_3 pollution, we further discussed the chemical budget of O_3 at different heights (Sect. 3.2.3), the vertical and temporal variability of $P(O_3)_{net}$ and O_3 formation regime (Sect. 3.2.4), along with potential bias within the modelling approach (Sect. 3.2.5).

3.2.1 Contribution of chemical and physical processes to O_3 changes on the ground level

As concluded in Sect. 3.1.1, O_3 pollution episodes may be jointly affected by the photochemical reactions and physical transport. In order to identify the main reasons for O_3 pollution on the ground level, we calculated the contribution of chemical and physical processes to O_X concentration changes at 5 m ground level separately for all 3 episodes and 2 non-episodes. Typically, as dry deposition contributes a relatively small portion and can often be considered negligible, making vertical and horizontal transport the main contributors to physical processes (Tan et al., 2019).

518
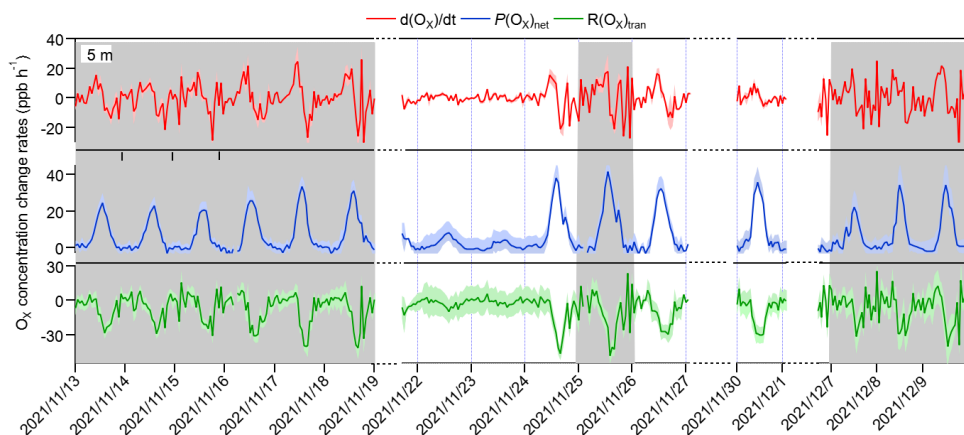
Figure 4. Time series of O_X concentration changes ($d(O_X)/dt$) and contributions from local photochemical production ($P(O_X)_{net}$) and physical transport ($R(O_X)_{tran}$). The shaded areas of $d(O_X)/dt$, $P(O_X)_{net}$, and $R(O_X)_{tran}$ represent one standard deviation (denoted by σ) of the mean $d(O_X)/dt$, the uncertainty of measured $P(O_X)_{net}$, and the propagated error of $R(O_X)_{tran}$, respectively.

519
520
521
522
523

524
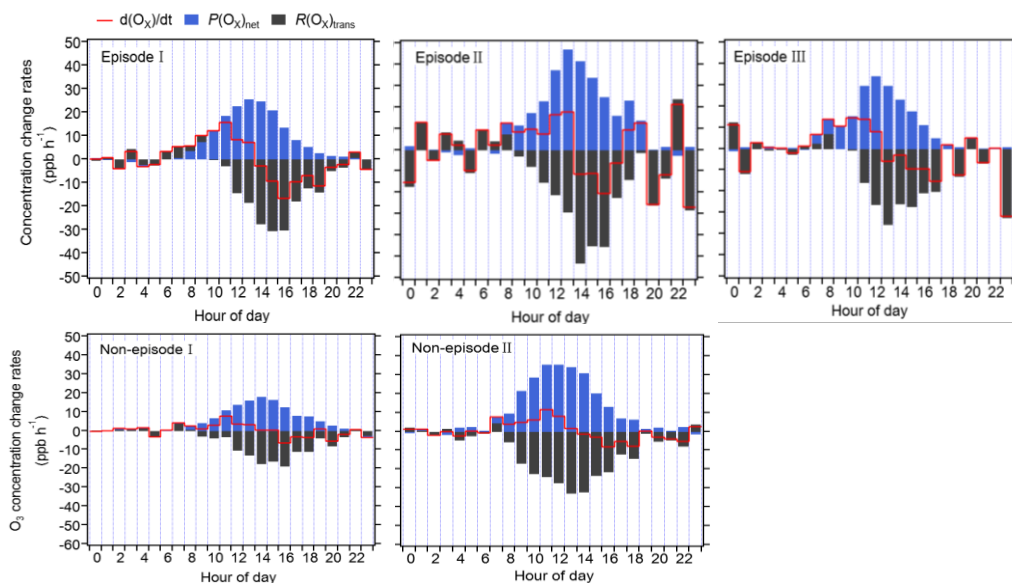
Figure 5. Diurnal variation of the contribution of chemical and physical transport to O_3 changes on the ground level.

525
526

$R(O_X)_{trans}$ at 5 m ground level was derived from $\frac{dO_X}{dt}$ manus $P(Ox)_{net}$, according to Eq. (5) shown Sect. 2.3.2, their hourly averages and diurnal variations are shown in Figs. 4 and 5, respectively. From these figures, it is evident that the fluctuation of the O_X concentration change rate ($d(O_X)/dt$) at ground level is typically small and primarily dominated by the physical processes during nighttime. During nighttime, $P(O_X)_{net}$ should be zero without sun radiation, the significant $P(O_X)_{net}$ shown in Fig. 5 may be

527
528
529
530
531
532

533   due to the measurement uncertainty of $P(O_X)_{net}$, which is determined by the

534   measurement error of O_X of CAPS-NO_2 monitor and the error caused by the light-

535   enhanced loss of O_3 in the reaction and reference chambers (as discussed in Sect. S4).

536   The measurement uncertainty of $P(O_X)_{net}$ is higher at lower $P(O_X)_{net}$ values (as shown

537   in Fig. 4), which was mainly determined by the instrumental error of O_X measurement

538   and the ambient O_X concentrations during nighttime. It was estimated to be ~ 38 % and

539   can be considered as the measurement precision. Around 6:00-7:00 LT, O_3

540   concentrations increase for all episodes and non-episodes, mainly due to physical

541   transport during episodes I and II and non-episodes I, while photochemical reactions

542   and physical processes are equally important for episodes III and non-episode II. This

543   could be due to short-term strong vertical turbulence in the early morning, which leads

544   to an expansion of the boundary layer height and makes the residual layer "leaky",

545   allowing vertical transport. At the same time, O_3 precursors were also transported down

546   from the residual layer, and with increasing sunlight, these O_3 precursors underwent

547   rapid photochemical reactions that competed with the physical processes between 6:00-

548   7:00 LT, leading to a sharp increase in $P(O_X)_{net}$ between 8:00 to 12:00 LT. The $P(O_X)_{net}$

549   peaked around 11:00-14:00 LT and started to decrease around 15:00, eventually

550   approaching zero by around 19:00-20:00 LT. Between 7:00-8:00 LT, $R(O_X)_{tran}>0$ for

551   all episodes and non-episodes, indicating inflow of O_3 from physical transport,

552   increasing surface O_3 concentration by averages of 4.7, 3.9, 2.3, 3.5, and 4.5 ppbv h^{-1}

553   for episodes I, II, III, and non-episodes I and II, respectively. From 9:00 to 10:00 LT,

554   $R(O_X)_{tran}>0$ only for episodes I, increasing the O_3 concentration by 1.5 ppbv h^{-1},

555   indicating inflow of O_3 from physical transport; on the contrary, $R(O_X)_{tran}<0$ for

556   episodes II and III, and non-episodes I and II, indicating outflow of O_3 from physical

557   transport, decreasing the O_3 concentration by 3.1, 0.1, 3.0, and 16.9 ppbv h^{-1},

558   respectively. After 10:00 LT, $R(O_X)_{tran}<0$ for all episodes and non-episodes, indicating

559   outflow of O_3 from the observation sites, possibly due to accumulated photochemically

560   formed O_3 increasing the concentration at the observation site, diffusing upward or to

561   surrounding areas.

562   In conclusion, the observed daytime O_3 concentration changes during all episodes

563   and non-episodes were influenced by both photochemical production and physical

564   transport. In the early morning, the increase in O_3 concentrations can be attributed to

565   photochemical reactions, physical processes, and possibly reduced NO titration effects

as the boundary layer height increases. Around noon, O_3 concentrations stabilize, suggesting a balance between photochemical reactions and physical transport affecting O_3 concentration changes. In the afternoon, O_3 concentrations decrease due to the transport of photochemically formed O_3 from the observation site to upward directions or the surrounding areas. Our findings indicate that local photochemical reactions dominate O_3 pollution. For example, O_3 pollution episodes recorded during the observation period manifest under specific conditions: ① high photochemical O_3 production (i.e., episode II); ② moderate photochemical O_3 productions coupled with O_3 accumulation under stable weather conditions (i.e., episodes I and III). In contrast, non-episodes observed during the observation period occur under different conditions: ① low levels of photochemical O_3 production (i.e., non-episodes I); ② elevated photochemical O_3 production, with O_3 transport to surrounding areas under favorable diffusion conditions (i.e., non-episodes II).

3.2.2 The model performance

In order to test the simulation ability of OBM-MCM model for $P(O_3)_{net}$, we compared the measured and modelled $P(O_3)_{net}$ at 5 m ground level, as depicted in Fig. S3a. The measured and modelled $P(O_3)_{net}$ revealed close alignment during episodes I and III, yet displayed discernible variations during episode II, non-episode I, and non-episode II. Assessment metrics including IOA, NMB, and NME were computed based on the observed and modelled $P(O_3)_{net}$ over the entire measurement period (as described in Sect. 2.3.3). The IOA ranged between 0.87 (25th percentile) and 0.90 (75th percentile) for the measured and modelled $P(O_3)_{net}$ across the measurement period, indicating the acceptable performance of the OBM-MCM model simulation (a higher IOA value signifies a stronger agreement between simulated and observed values). Additionally, comparison of measured and modelled O_3 concentrations at different heights (as shown in Fig. S4) revealed generally higher modelled values during daytime and closer alignment during nighttime at lower heights (i.e., 5 m, 40 m, and 70 m), while discrepancies were observed at higher heights (i.e., 120 m, 220 m, and 335 m). These phenomena may be primarily attributed to uncertainties in assumed physical processes in the modelling, such as vertical and horizontal transport. Previous studies have utilized the comparison of measured and modelled O_3 concentrations to determine the dilution factor in modelling studies, discovering that suitable dilution factors vary by location (Yang et al., 2021). To achieve the best agreement between the modelled O_3

concentrations and the observed values, we applied different dilution factors (the lifetime of the species) in the modelling, varying from 6 h to 24 h. We found that the simulated O_3 is closest to the measured O_3 concentrations when the lifetime of the species is set to 12 h. However, given that O_3 concentrations are affected by physical transport processes, the dilution factor might only represent the outflow of O_3 from the observation site. Therefore, there may be limitations in using this method for precise comparisons. We further compared the measured and modelled $P(O_3)_{net}$ under different dilution factors. The modelled $P(O_3)_{net}$ initially increases and then decreases as the dilution factor decreases (equivalent to an increase of species lifetime). However, the influence of varying dilution rates on the modelled $P(O_3)_{net}$ is minimal, constituting less than 30 %, due to the short lifetimes of the HO_2 and RO_2 radicals, which determine the $P(O_3)_{net}$ values (Wang et al., 2021). Notably, the modelled $P(O_3)_{net}$ closely matched the measured values when the species lifetime was set to12 h, as illustrated in Fig. S3b. Consequently, a constant dilution factor of $1/43200$ s^{-1} was applied throughout the observation period. Further investigations revealed an IOA range between 0.80 (25th percentile) and 0.82 (75th percentile) for measured and modelled O_3 concentrations at 5 m ground level, which lies in between the IOA result for the modelled and observed O_3 concentrations in previous studies, which range between 0.68 and 0.89 (Wang et al., 2018), signifying the modelling results for O_3 concentrations here are acceptable. The calculated NMB and NME using the modelled and observed $P(O_3)_{net}$ at 5 m ground level during the whole measurement period ranged from -0.42 (25th percentile) to -0.31 (75th percentile) and -0.42 (25th percentile) to 0.54 (75th percentile), respectively. These analysis results indicate that the model underestimates the measured $P(O_3)_{net}$ by a factor ranging from 1.42 (25th percentile) to 1.31 (75th percentile), calculated as (1+|NMB|), and the simulation results are reliable (with -1<NME<1).

The mean diel variation of measured and modelled $P(O_3)_{net}$ during different episodes and non-episodes are shown in Fig. 6a-e. The maximum daily $P(O_3)_{net}$ values were 29.3, 47.2, and 34.2 ppbv h^{-1} for episodes I, II, and III, and 17.9 and 35.5 ppbv h^{-1} for non-episodes I and II, respectively. These values were comparable to or lower than those measured in urban areas of Houston, United States (40-50 and 100 ppbv h^{-1} in autumn and spring, respectively) (Baier et al., 2015; Ren et al., 2013), but higher than those measured in a remote area of Japan (10.5 ppbv h^{-1} in summer) and an urban area of Pennsyvania, United States (~ 8 ppbv h^{-1} in summer) (Sadanaga et al., 2017; Cazorla

and Brune, 2020). The averaged diel profiles of measured and simulated $P(O_3)_{net}$ exhibited large standard deviations (as depicted in Table 1), representing their day-to-day variation throughout the campaign. The measured $P(O_3)_{net}$ were mostly higher than the modelled $P(O_3)_{net}$, which could be attributed to the underestimation of RO_2 under high NO conditions, leading to substantial disparities between calculated $P(O_3)_{net}$ derived from measured and modelled RO_2 concentrations, as highlighted in previous studies (Whalley et al., 2018, 2021; Tan et al., 2017, 2018). The median value of [measured $P(O_3)_{net}$-modelled $P(O_3)_{net}$]/measured $P(O_3)_{net}$ ranged from 22% to 45% for different episodes and non-episodes. To delve deeper, we further investigated the relationship between the daily disparities of measured and modelled $P(O_3)_{net}$ ($\Delta P(O_3)_{net}$ = measured $P(O_3)_{net}$-modelled $P(O_3)_{net}$) and average daytime NO concentrations during different episodes and non-episodes, as depicted in Fig. 6f. The observed elevated $\Delta P(O_3)_{net}$ at higher NO concentrations aligns with findings from previous studies, which suggest that multiple factors could contribute to these outcomes. For example, the reaction of OH with unknown VOCs (Tan et al., 2017), the lack of correction for the decomposition of $CH_3O_2NO_2$, the missing RO_2 production from photolysis $ClNO_2$ (Whalley et al., 2018; Tan et al., 2017), and the underestimation of OVOCs photolysis (Wang et al., 2022b) in modelling approaches may lead to the underestimation of RO_2, thus underestimating the modelled $P(O_3)_{net}$. Further analysis showed that the underestimation of $P(O_3)_{net}$ can lead to the NOx-limited regime being shifted to the VOCs-limited regime, thus underestimating the NOx-limited regime (Wang et al., 2022b, 2024). However, the derived IOA, NMB, and NME values from the modelled and observed $P(O_3)_{net}$ (and O_3) at 5 m ground during different episodes and non-episodes indicate that the model proficiently reproduces the genuine $P(O_3)_{net}$ at the observation site (as shown in Table S3). Consequently, these results provide confidence in exploring the vertical and temporal variations of $P(O_3)_{net}$ and O_3 formation sensitivities utilizing the outcomes from the modelling approach. Nonetheless, it is important to acknowledge and discuss the potential biases caused by the modelling methodology in this study.
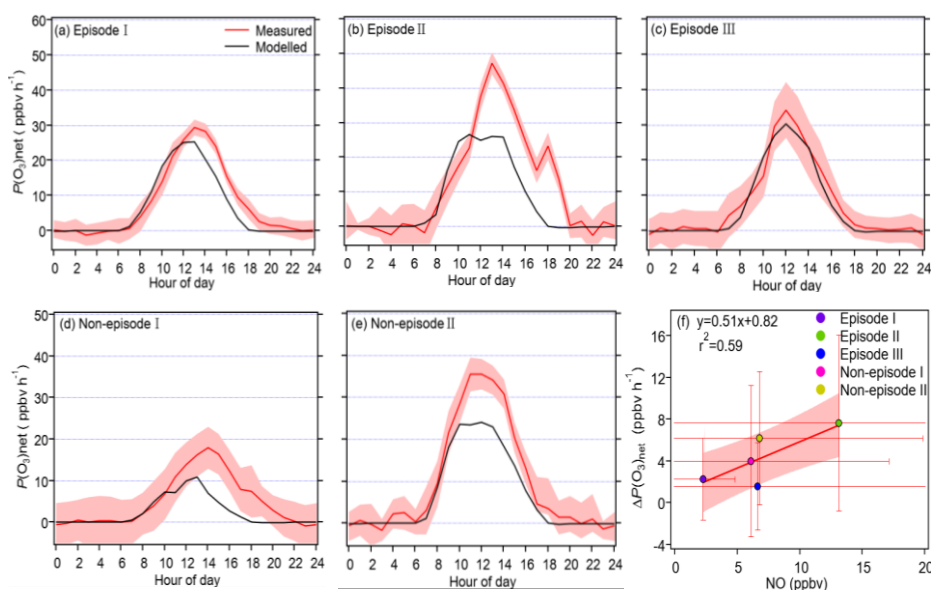
Figure 6. (a-e) diurnal variations of the measured and modelled $P(O_3)_{net}$ during the observation period, and (f) the relationship between the average daily differences of measured and modelled $P(O_3)_{net}$ ($\Delta P(O_3)_{net}$) and the average daytime NO concentrations during different episodes and non-episodes.

3.2.3 Vertical and temporal variability of $P(O_3)_{net}$ budget

The detailed $P(O_3)_{net}$ budget at different heights during the observation period from the modelling results are shown in Fig. 7. Across various heights and different episodes and non-episodes, the contributions of different reaction pathways to $P(O_3)$ were almost the same, with HO_2+NO as the major O_3 production pathway, followed by CH_3O_2+NO and other RO_2+NO, where other RO_2+NO encompasses all RO_2 except CH_3O_2. This result aligns with previous studies (Liu et al., 2021; Liu et al., 2022). The major O_3 destruction pathway was $OH+NO_2$ (loss of OH radicals), followed by net RO_2+NO_2 (form peroxyacetyl nitrate, commonly called PAN species) and O_3 photolysis, while other O_3 destruction pathways, including O_3+OH, O_3+HO_2, $C_5H_8+O_3$, $C_3H_6+O_3$, and $C_2H_4+O_3$, together contributed negligibly to O_3 destruction. These $P(O_3)$ and $D(O_3)$ reaction pathways occurred between 6:00-18:00 LT, exhibiting strong diurnal variation characterized by a sharp increase between 6:00-11:00 LT in the morning, peaking between 11:00 and 14:00 LT, and decreasing rapidly after 14:00 LT. These phenomena were in accordance with the concentration changes of the major oxidants (i.e., OH, O_3, and NO_3), as shown in Fig. S5, where OH radicals and O_3 concentrations increased significantly in the morning and reached a peak around noon, followed by sharp afternoon decreases.

687   The diurnal changes in the concentrations of different reaction pathways to $P(O_3)$

688   and $D(O_3)$ at 5 m ground level during different episodes and non-episodes are depicted

689   in Fig. S6. We note that the maximum total $P(O_3)$ resulting from diel variations at 5 m

690   ground level for episode I, II, and III were 32.0, 34.9, and 38.3 ppbv h^{-1}, respectively.

691   These values were consistently higher than the maximum total $P(O_3)$ observed for non-

692   episodes I and II, which were 15.6 and 30.7 ppbv h^{-1}, respectively. However, as $P(O_3)_{net}$

693   was determined by both $P(O_3)$ and $D(O_3)$, the maximum total $D(O_3)$ values resulting

694   from diel variations during episodes I, II, III, and non-episode I, II, were 5.0, 5.7, 5.1,

695   2.4, and 5.3 ppbv h^{-1}, respectively. Consequently, the modelled $P(O_3)_{net}$ during episodes

696   does not exhibiting a statistically significant difference from that during non-episodes

697   (Mann-Whitney p value=0.12), as shown in Fig. S5, which is in agreement with the

698   measured $P(O_3)_{net}$ (Mann-Whitney p-value=0.28), as depicted in Sect. 3.1.1.

699   The diurnal variation of $P(O_3)_{net}$ during different episodes and non-episodes

700   obtained by OBM-MCM modelling at different heights are shown in Fig. 8. We saw

701   that the $P(O_3)_{net}$ all showed a decreasing trend with the increase of the measurement

702   height during different episodes and non-episodes, but the variation of $P(O_3)_{net}$ along

703   with the measurement height differed for different episodes and non-episodes. For

704   example, the decrement of the averaged $P(O_3)_{net}$ during 6:00-18:00 LT from 5 m to 335

705   m were 1.5 and 0.6 ppbv h^{-1} for episode I and non-episode I, respectively, which was

706   relatively smaller than that during episode II, episode III, and non-episode II, which

707   were 5.3, 5.4, and 4.0 ppbv h^{-1}, respectively. To explore the reason, we plotted the

708   differences of calculated OH reactivities at 5 m and 335 m of different VOCs groups

709   (marked as ΔOH reactivity) as a function of the $P(O_3)_{net}$ change at 5 m and 335 m

710   (marked as Δ$P(O_3)_{net}$), including nonmethane hydrocarbons (NMHC), anthropogenic

711   volatile organic compounds (AVOC), biogenic volatile organic compounds (BVOC),

712   and oxygenated volatile organic compounds (OVOC) (as shown in Fig.8f). The VOCs

713   species included in each category are listed in Table S2. We found that the OH

714   reactivities of AVOC and OVOC had the highest correlation coefficients (R^2) with the

715   Δ$P(O_3)_{net}$, which are 0.85 and 0.67, respectively, indicating their predominant influence

716   on the decrement of $P(O_3)_{net}$ from 5 m to 335 m. However, the OH reactivity change

717   from 5 m to 335 m of different groups was quite different. Therefore, we further

718   explored O_3 formation sensitivity to its different VOCs precursors and precursor groups.

719

720
721
722
723
724
725
726
727
728
729
730
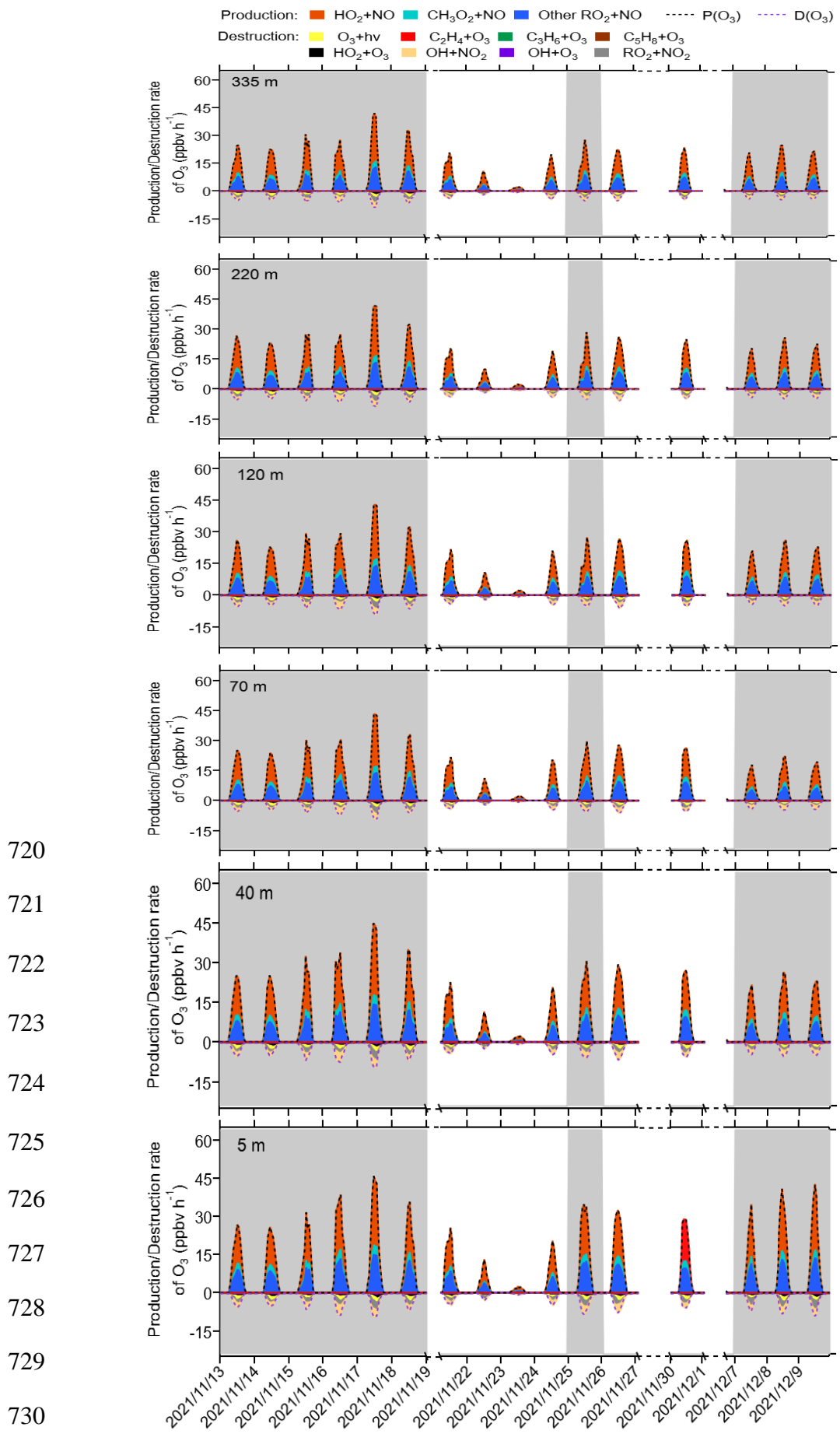
     Figure 7. Time series of model-simulated O₃ production and destruction rates during 13

     November and 9 December 2021, at different heights at SZMGT, the gray columns show the

     typical O₃ episodes that occurred.
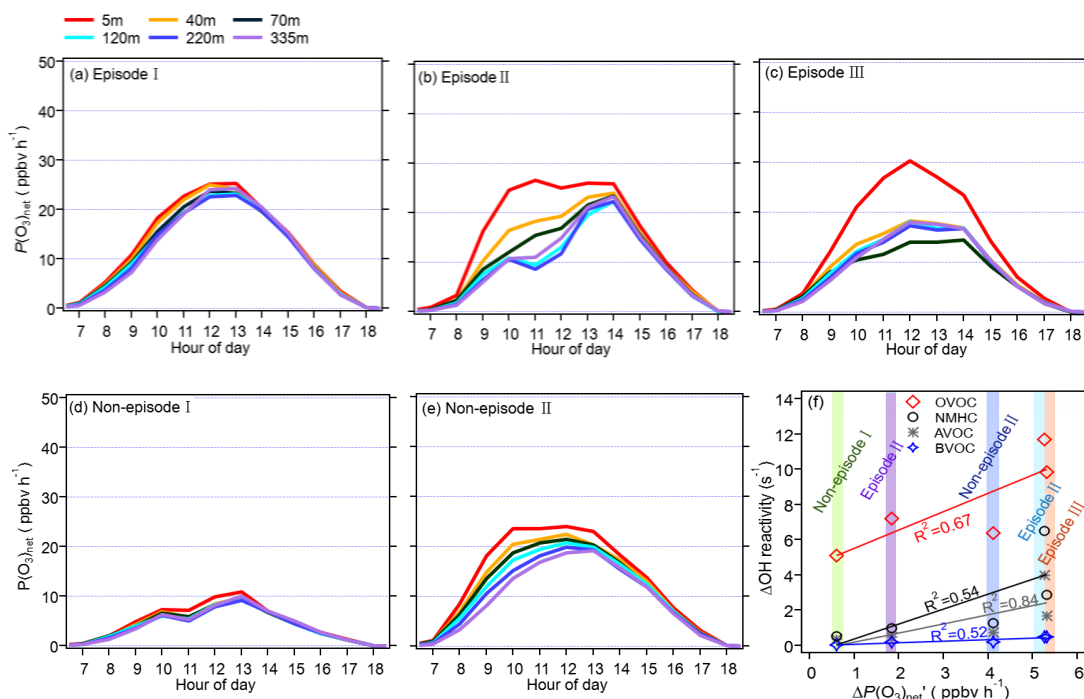
734

735   **Figure 8. (a-e) Diurnal variation of vertical profile of the model-simulated $P(O_3)_{net}$**

736   **during different episodes and non-episodes from 13 November to 9 December 2021, and (f)**

737   **the relationship between the average daytime differences of modelled $P(O_3)_{net}$ (denoted as**

738   **$\Delta P(O_3)_{net}$), and OH reactivity of different precursor groups at 5 m and 335 m (denoted as ΔOH**

739   **reactivity).**

740   ### 3.2.4   Vertical distributions of O₃ formation regime

741   To investigate the reasons behind the variable distribution of $P(O_3)_{net}$ at varying

742   heights, we clarified the sensitivity of O₃ formation to different O₃ precursors or

743   precursor groups, including NMHC, AVOC, BVOC, OVOC, CO, and NOx, by

744   calculating their RIRs during different episodes and non-episodes, as shown in Fig. 9.

745   The VOCs species, categorized into different precursor groups as listed in Table S2,

746   indicate that some species depicted in Figure 9 may appear in multiple categories and

747   hence could be repeated. As illustrated in Fig. 9, the RIR values for different O₃-

748   precursors or precursor groups don't exhibit significant variation at different heights

749   during specific episodes or non-episodes, indicating a similar photochemical O₃

750   formation regime. However, the O₃ formation regimes differ between different episodes

751   or non-episodes. During O₃ polluted episode I, O₃ formation is located in a transition

752 regime and is more sensitive to VOCs emissions. Conversely, during O_3 polluted

753 episodes II and III, and non-episodes I and II, it is located in VOCs sensitive regime.

754 This finding aligns with previous studies suggesting that photochemical O_3 formation

755 in the PRD region is likely VOC-limited or mixed-limited (Hong et al., 2022; Lu et al.,

756 2018). The results suggest that the complexity of O_3 mitigation at the observation site.

757 For example, during polluted episode I, reducing both VOCs and NOx can mitigate

758 photochemical O_3 formation. However, during other O_3 polluted episodes and non-

759 episodes, reducing VOCs can effectively alleviate photochemical O_3 formation, while

760 reducing NOx might aggravate it. Nevertheless, during all episodes and non-episodes,

761 O_3 formation is most sensitive to AVOC (RIR: 0.83-1.12), followed by OVOC (RIR:

762 0.59-0.79) at different heights, indicating the urgent need to reduce AVOC and OVOC

763 emissions to mitigate O_3 pollution in this area.
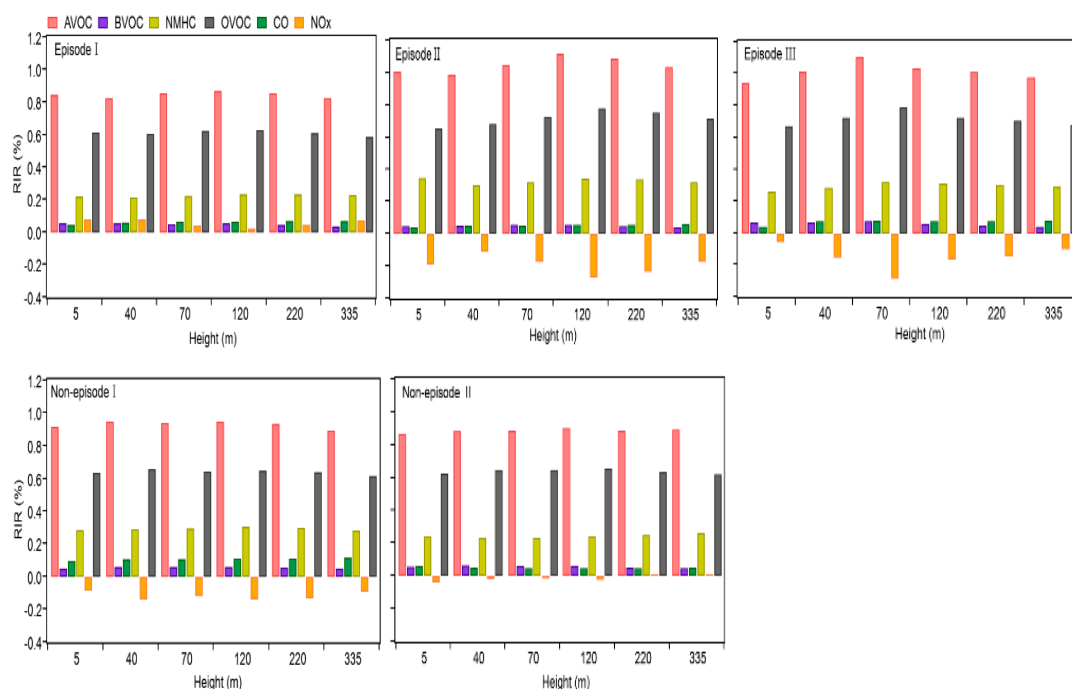
765 **Figure 9. RIR values for O_3-precursor or precursor groups at different heights during**

766 **different classified episodes.**

767   The RIR tests for different episodes and non-episodes at various hours of the local

768 daytime are illustrated in the Supplement (Fig. S7). The results indicate that the diurnal

769 changes of RIR values for different episodes and non-episodes exhibit remarkable

770 similarities. In the morning, the RIR values for various VOC groups, including AVOC,

771 BVOC, OVOC, and CO, are typically higher than those for NOx. However, they

772 gradually decrease throughout the day until 16:00 LT, then increase and reach a peak

773 at 18:00 LT. Interestingly, the RIR values at this peak are lower than those at 8:00 LT

774 in the morning. Conversely, the RIR values for NOx are usually around zero or below

775 zero during most of the day, gradually increasing around 16:00 LT and peaking at 18:00

776 LT. This suggests a transition in the photochemical O_3 formation regime throughout

777 the day, shifting from a VOC-limited regime in the morning to a transition regime and

778 more sensitive to NOx in the afternoon around 16:00 LT. The diurnal variations of the

779 RIRs of different O_3 precursors or precursor groups offer detailed insights into the

780 dominant factors influencing the photochemical formation of O_3 at different times of a

781 day.

782 Through the sensitivity study, NOx is not found to be the limiting factor affecting

783 $P(O_3)_{net}$, therefore, reactions involving NOx in the ROx radicals cycle, such as

784 $RO_2+NO \rightarrow HO_2$ and $HO_2+NO \rightarrow OH$, should occurred efficiently. Conversely,

785 reactions not involving NOx, such as $OH+VOCs \rightarrow RO_2$, should be the limiting steps of

786 the ROx radicals cycling. Given that photochemical O_3 formation is most sensitive to

787 AVOC and OVOC groups, we further identified and presented the three VOC species

788 with the highest OFP during different episodes and non-episodes in Table S4. Results

789 show that compounds such as toluene, *m/p*-xylene, and n-butane in AVOC group,

790 formaldehyde, hydroxyacetone, and ethanol in OVOC group have identified as the most

791 significant contributors to the total OFP in all episodes and non-episodes. Toluene, *m/p*-

792 xylene, and n-butane are often associated with specific industrial processes (Shi et al.,

793 2022; Liang et al., 2017), while formaldehyde, hydroxyacetone, and acetaldehyde can

794 originate from both the industrial processes and natural sources (Parrish et al., 2012;

795 Fan et al., 2021; Spaulding et al., 2003; Salthammer 2023). Priority of these emission

796 sources should be given to reducing AVOC and OVOC to mitigate O_3 pollution in the

797 PRD area of China.

798 **4 Conclusions**

799 We carried out a field observation campaign in an urban area in Pearl River Delta

800 (PRD) in China, focusing on investigating the vertical temporal variability of near-

801 surface O_3 production mechanisms by using a newly built vertical observation system

802 and the observation-based model coupled to the Master Chemical Mechanism (OBM-

803 MCM) v3.3.1. In total, three O_3 pollution episodes and two non-episodes occured

804 during the observation period. To assess the modelling performance for O_3 production

805   rates and sensitivity, as well as to investigate the potential reasons for O_3 pollution

806   episodes at 5 m ground level, a net photochemical O_3 production rate (NPOPR, $P(O_3)_{net}$)

807   detection system based on the current dual-channel reaction chamber technique was

808   employed to directly measure $P(O_3)_{net}$ at 5 m ground-level.

809   The vertical profiles of averaged concentrations of various pollutants exhibit

810   similar trends during both episodes and non-episodes. The O_3, NOx, and Ox

811   concentrations show minimal vertical gradient during the daytime due to rapid vertical

812   mixing effects, but distinct vertical gradients emerge during nighttime owing to the

813   stability of the nocturnal residual layer. Higher concentrations of O_3 and Ox were

814   observed at higher heights, while elevated NO and NOx concentrations were mainly

815   detected at ground level. Given that NO has a significant titration effect on O_3, the lower

816   O_3 concentration at ground level may be attributed to the increase in NOx concentration

817   due to a more pronounced NO titration effect, besides the dry deposition near the

818   ground. However, the TVOC and their OFP exhibited variable trends with increased

819   height during both daytime and nighttime, observed in episodes and non-episodes,

820   which indicates the complexities of O_3 formation mechanisms at different heights

821   throughout the atmospheric column. Total OFP was highest at the 5 m ground level and

822   exhibited higher levels during episodes compared to non-episode periods. The OFP was

823   primarily attributed to OVOCs at different altitudes throughout both episodes and non-

824   episodes.

825   The mean concentrations of O_3 precursors, including CO, NO, NO_2, and TVOC,

826   were not consistently elevated during episodes compared to their levels during non-

827   episodes. By considering the observed O_3 concentrations change and the measured

828   $P(O_3)_{net}$ at 5 m ground level, we found that the O_3 pollution episodes were influenced

829   by both photochemical production and physical transport, with local photochemical

830   reactions playing a key role. O_3 pollution episodes recorded during the observation

831   period occured under specific conditions: ① high photochemical O_3 productions; ②

832   moderate photochemical O_3 productions coupled with O_3 accumulation under stable

833   weather conditions. The index of agreement (IOA) ranged from 0.87 (25th percentile)

834   to 0.90 (75th percentile) for the measured and modelled $P(O_3)_{net}$ across the measurement

835   period, indicating the rationality to investigate the vertical and temporal variability of

836   O_3 formation mechanisms using modelling results. However, the measured $P(O_3)_{net}$

837   generally exceeded the modelled $P(O_3)_{net}$, the differences between measured and

838 modelled $P(O_3)_{net}$ ($\Delta P(O_3)_{net}$) were found to be correlated with NO concentrations. Base

839 on previous studies, this phenomenon could potentially be attributed to the

840 underestimation of RO_2 at high NO conditions, arising from inadequate knowledge

841 concerning photochemical reaction mechanisms. Therefore, the potential biases caused

842 by the modelling methodology were acknowledged and discussed.

843   From the modelling results, the contribution of different reaction pathways to $P(O_3)$

844 was almost the same at varying heights during both episodes and non-episodes, with

845 HO_2+NO as the major O_3 production pathway, followed by other RO_2+NO (comprising

846 all RO_2 except CH_3O_2) and CH_3O_2+NO. The major O_3 destruction pathway was

847 $OH+NO_2$ (loss of OH radicals), followed by net RO_2+NO_2 (forming peroxyacetyl

848 nitrate) and O_3 photolysis. However, other O_3 destruction pathways, including O_3+OH,

849 O_3+HO_2, $C_5H_8+O_3$, $C_3H_6+O_3$, and $C_2H_4+O_3$, collectively contributed negligibly to O_3

850 destruction. Nevertheless, $P(O_3)_{net}$ showed a decreasing trend with the increase of

851 height during different episodes and non-episodes, which was found mainly attributed

852 to the decline in O_3 precursor concentrations, specifically anthropogenic organic

853 compounds (AVOC) and oxygenated volatile organic compounds (OVOC) groups. We

854 observed that modelling biases were correlated with NO concentrations and VOCs

855 categories, impacting $P(O_3)_{net}$ through the regulation of the RO_2 radicals' budget. The

856 median relative difference between measured and modelled $P(O_3)_{net}$ ranged from 22-

857 45 % during different episodes and non-episodes. Therefore, the variation of $P(O_3)_{net}$

858 along with the measurement height might be even larger than our initial assessment.

859   Similar photochemical O_3 formation regimes were observed at different heights

860 during specific episodes or non-episodes, yet they varied between different episodes or

861 non-episodes. O_3 formation was predominantly located at a transition regime and more

862 sensitive to VOCs emissions during O_3-polluted episode I, whereas it shifted to a

863 VOCs-sensitive regime during O_3-polluted episodes II and III, as well as non-episodes

864 I and II. Further analysis revealed a daytime shift in the photochemical O_3 formation

865 regime, transitioning from a VOC-limited regime in the morning to a transition regime

866 more sensitive to NOx round 16:00 LT in the afternoon. However, the underestimation

867 of RO_2 radicals in the modelling, especially at lower heights with higher NO

868 concentrations, could result in an overestimate of the VOCs-limited regime. This study

869 highlights the need for more precise analysis using direct measurement techniques in

870 future studies. Nonetheless, throughout all episodes and non-episodes, O_3 formation is

most sensitive to AVOC, followed by OVOC at various heights, emphasizing the urgent need to reduce emissions of these compounds to mitigate O_3 pollution in this area.

This is the first measurement report of the vertical-temporal of O_3 formation mechanisms near the ground surface. Together with the deliberation of the possible bias on the vertical-temporal profile of O_3 formation rate and sensitivity using modelling studies, this research provides critical foundational insights. The findings provide us in-depth understanding of near-ground vertical variability in O_3 formation mechanisms, which are influenced by the concentrations of VOCs and NOx, and the distinct OFP associated with different VOCs profiles. During daytime, the vertical mixing of air masses is substantially enhanced due to the effect of surface heating. Consequently, photochemically formed O_3 at higher altitudes can be vertically transported downward to the near-ground layer. Under this condition, control strategies for O_3 precursors based on the O_3 formation mechanisms on the ground-level are insufficient. A more comprehensive approach is necessary to effectively address the complexities of O_3 production throughout the atmospheric column. The vertical variability of O_3 formation mechanisms should be taken into account when making effective O_3 control strategies in the PRD area of China.

Data availability. Data related to this article are available online *at* https://zenodo.org/records/10473104.

Author contributions. BY, JZ, XBL, and MS designed the experiment, YXH and JZ performed the $P(O_3)_{net}$ measurement, BY and XBL built the vertical observation system based on SZMGT. JZ, CZ, AL, BY, JPZ, YXH, YW, XBL, XJH, XS, YC, SY, SY, YW, JPQ collected and analysed the data. JZ wrote the manuscript, all authors revised the manuscript.

Competing interests. The authors declare that they have no known competing interests.

Acknowledgements. This study was funded by the Key-Area Research and Development Program of Guangdong Province (grant no. 2020B1111360003), the National Natural Science Foundation of China (No. 42305096), and the Natural Science Foundation of Guangdong Province (grant no. 2020A1515110526).

References

Anenberg, S. C., Schwartz, J., Shindell, D., Amann, M., Faluvegi, G., Klimont, Z., Janssens-Maenhout, G., Pozzoli, L., Van Dingenen, R., Vignati, E., Emberson, L., Muller, N. Z., West, J. J., Williams, M., Demkine, V., Hicks, W. K., Kuylenstierna, J., Raes, F., and Ramanathan, V.: Global air quality and health co-benefits of mitigating near-term climate change through methane and black carbon emission controls, Environ. Health. Perspect., 120, 831-839, 10.1289/ehp.1104301, 2012.

Baier, B. C., Brune, W. H., Lefer, B. L., Miller, D. O., and Martins, D. K.: Direct ozone production rate measurements and their use in assessing ozone source and receptor regions for Houston in 2013, Atmos. Environ., 114, 83-91, 10.1016/j.atmosenv.2015.05.033, 2015.

Benish, S. E., He, H., Ren, X., Roberts, S. J., Salawitch, R. J., Li, Z., Wang, F., Wang, Y., Zhang, F., Shao, M., Lu, S., and Dickerson, R. R.: Measurement report: Aircraft observations of ozone, nitrogen oxides, and volatile organic compounds over Hebei Province, China, Atmos. Chem. Phys., 20, 14523-14545, 10.5194/acp-20-14523-2020, 2020.

Carter, W. P. L. and Heo G. (2012): Development of Revised SAPRC Aromatics Mechanisms, Report to the California Air Resources Board Contracts No. 07-730 and 08-326, April 12, 2012. Available at: http://www.cert.ucr.edu/~carter/absts.htm#saprc11, 2012.

Cazorla, M. and Brune, W. H.: Measurement of ozone production sensor, Atmos. Meas. Tech., 3, 545-555, 10.5194/amt-3-545-2010, 2010.

Decker, Z. C. J., Zarzana, K. J., Coggon, M., Min, K.-E., Pollack, I., Ryerson, T. B., Peischl, J., Edwards, P., Dubé, W. P., Markovic, M. Z., Roberts, J. M., Veres, P. R., Graus, M., Warneke, C., de Gouw, J., Hatch, L. E., Barsanti, K. C., and Brown, S. S.: Nighttime chemical transformation in biomass burning plumes: a box model analysis initialized with aircraft observations, Environ. Sci. Technol., 53, 2529-2538, 10.1021/acs.est.8b05359, 2019.

Fan, J., Ju, T., Wang, Q., Gao, H., Huang, R., and Duan, J.: Spatiotemporal variations and potential sources of tropospheric formaldehyde over eastern China based on OMI satellite data, Atmos. Pollut. Res., 12, 272-285, 10.1016/j.apr.2020.09.011, 2021.

933   Fiore, A. M., Dentener, F. J., Wild, O., Cuvelier, C., Schultz, M. G., Hess, P.,
934 Textor, C., Schulz, M., Doherty, R. M., Horowitz, L. W., MacKenzie, I. A., Sanderson,
935 M. G., Shindell, D. T., Stevenson, D. S., Szopa, S., Van Dingenen, R., Zeng, G.,
936 Atherton, C., Bergmann, D., Bey, I., Carmichael, G., Collins, W. J., Duncan, B. N.,
937 Faluvegi, G., Folberth, G., Gauss, M., Gong, S., Hauglustaine, D., Holloway, T.,
938 Isaksen, I. S. A., Jacob, D. J., Jonson, J. E., Kaminski, J. W., Keating, T. J., Lupu, A.,
939 Marmer, E., Montanaro, V., Park, R. J., Pitari, G., Pringle, K. J., Pyle, J. A., Schroeder,
940 S., Vivanco, M. G., Wind, P., Wojcik, G., Wu, S., and Zuber, A.: Multimodel estimates
941 of intercontinental source-receptor relationships for ozone pollution, J. Geophys. Res.,
942 114, 10.1029/2008jd010816, 2009.

943   Geng, C., Wang, J., Yin, B., Zhao, R., Li, P., Yang, W., Xiao, Z., Li, S., Li, K.,
944 and Bai, Z.: Vertical distribution of volatile organic compounds conducted by tethered
945 balloon in the Beijing-Tianjin-Hebei region of China, J. Environ. Sci., 95, 121-129,
946 10.1016/j.jes.2020.03.026, 2020.

947   Hao, Y., Zhou, J., Zhou, J. P., Wang, Y., Yang, S., Huangfu, Y., Li, X. B., Zhang,
948 C., Liu, A., Wu, Y., Zhou, Y., Yang, S., Peng, Y., Qi, J., He, X., Song, X., Chen, Y.,
949 Yuan, B., and Shao, M.: Measuring and modeling investigation of the net
950 photochemical ozone production rate via an improved dual-channel reaction chamber
951 technique, Atmos. Chem. Phys., 23, 9891-9910, 10.5194/acp-23-9891-2023, 2023.

952   Hong, Q., Zhu, L., Xing, C., Hu, Q., Lin, H., Zhang, C., Zhao, C., Liu, T., Su, W.,
953 and Liu, C.: Inferring vertical variability and diurnal evolution of O_3 formation
954 sensitivity based on the vertical distribution of summertime HCHO and NO_2 in
955 Guangzhou, China, Sci. Total Environ., 827, 10.1016/j.scitotenv.2022.154045, 2022.

956   Jenkin, M. E., Young, J. C., and Rickard, A. R.: The MCM v3.3.1 degradation
957 scheme for isoprene, Atmos. Chem. Phys., 15, 11433-11459, 10.5194/acp-15-11433-
958 2015, 2015.

959   Klein, A., Ravetta, F., Thomas, J. L., Ancellet, G., Augustin, P., Wilson, R.,
960 Dieudonné, E., Fourmentin, M., Delbarre, H., and Pelon, J.: Influence of vertical mixing
961 and nighttime transport on surface ozone variability in the morning in Paris and the
962 surrounding region, Atmos. Environ., 197, 92-102, 10.1016/j.atmosenv.2018.10.009,
963 2019.

Li, X.-B., Yuan, B., Wang, S., Wang, C., Lan, J., Liu, Z., Song, Y., He, X., Huangfu, Y., Pei, C., Cheng, P., Yang, S., Qi, J., Wu, C., Huang, S., You, Y., Chang, M., Zheng, H., Yang, W., Wang, X., and Shao, M.: Variations and sources of volatile organic compounds (VOCs) in urban region: insights from measurements on a tall tower, Atmos. Chem. Phys., 22, 10567-10587, 10.5194/acp-22-10567-2022, 2022.

Li, X.-B., Zhang, C., Liu, A., Yuan, B., Yang, H., Liu, C., Wang, S., Huangfu, Y., Qi, J., Liu, Z., He, X., Song, X., Chen, Y., Peng, Y., Zhang, X., Zheng, E., Yang, L., Yang, Q., Qin, G., Zhou, J., and Shao, M.: Assessment of long tubing in measuring atmospheric trace gases: applications on tall towers, Environ. Sci.: Atmos., 3, 506-520, 10.1039/d2ea00110a, 2023.

Li, Y., Liu, B., Ye, J., Jia, T., Khuzestani, R. B., Sun, J. Y., Cheng, X., Zheng, Y., Li, X., Wu, C., Xin, J., Wu, Z., Tomoto, M. A., McKinney, K. A., Martin, S. T., Li, Y. J., and Chen, Q.: Unmanned aerial vehicle measurements of volatile organic compounds over a subtropical forest in China and implications for emission heterogeneity, ACS. Earth. Space. Chem., 5, 247-256, 10.1021/acsearthspacechem.0c00271, 2021.

Liang, X., Chen, X., Zhang, J., Shi, T., Sun, X., Fan, L., Wang, L., and Ye, D.: Reactivity-based industrial volatile organic compounds emission inventory and its implications for ozone control strategies in China, Atmos. Environ., 162, 115-126, 10.1016/j.atmosenv.2017.04.036, 2017.

Liu, J., Liu, Z., Ma, Z., Yang, S., Yao, D., Zhao, S., Hu, B., Tang, G., Sun, J., Cheng, M., Xu, Z., and Wang, Y.: Detailed budget analysis of HONO in Beijing, China: Implication on atmosphere oxidation capacity in polluted megacity, Atmos. Environ., 244, 117957, 10.1016/j.atmosenv.2020.117957, 2021.

Liu, T., Hong, Y., Li, M., Xu, L., Chen, J., Bian, Y., Yang, C., Dan, Y., Zhang, Y., Xue, L., Zhao, M., Huang, Z., and Wang, H.: Atmospheric oxidation capacity and ozone pollution mechanism in a coastal city of southeastern China: analysis of a typical photochemical episode by an observation-based model, Atmos. Chem. Phys., 22, 2173-2190, 10.5194/acp-22-2173-2022, 2022.

Liu, X., Wang, N., Lyu, X., Zeren, Y., Jiang, F., Wang, X., Zou, S., Ling, Z., and Guo, H.: Photochemistry of ozone pollution in autumn in Pearl River Estuary, South

995   China, Sci. Total Environ., 754, 141812, 10.1016/j.scitotenv.2020.141812, 2021.

996   Liu, Z., Zha, F., Wang, Y., Yuan, B., Liu, B., and Tang, G.: Vertical evolution of
997   the concentrations and sources of volatile organic compounds in the lower boundary
998   layer in urban Beijing in summer, Chemosphere, 332, 138767,
999   10.1016/j.chemosphere.2023.138767, 2023.

1000   Lu, X., Hong, J., Zhang, L., Cooper, O. R., Schultz, M. G., Xu, X., Wang, T., Gao,
1001   M., Zhao, Y., and Zhang, Y.: Severe surface ozone pollution in China: a global
1002   perspective, Environ. Sci. Technol. Lett., 5, 487-494, 10.1021/acs.estlett.8b00366,
1003   2018.

1004   Luo, Y., Dou, K., Fan, G., Huang, S., Si, F., Zhou, H., Wang, Y., Pei, C., Tang, F.,
1005   Yang, D., Xi, L., Yang, T., Zhang, T., and Liu, W.: Vertical distributions of
1006   tropospheric formaldehyde, nitrogen dioxide, ozone and aerosol in southern China by
1007   ground-based MAX-DOAS and LIDAR measurements during PRIDE-GBA 2018
1008   campaign, Atmos. Environ., 226, 10.1016/j.atmosenv.2020.117384, 2020a.

1009   Luo, Y. P., Fu, J. Y., Li, Q. S., Chan, P. W., and He, Y. C.: Observation of Typhoon
1010   Hato based on the 356-m high meteorological gradient tower at Shenzhen, J. Wind. Eng.
1011   Ind. Aerodyn., 207, 104408, 10.1016/j.jweia.2020.104408, 2020b.

1012   Mao, J., Yan, F., Zheng, L., You, Y., Wang, W., Jia, S., Liao, W., Wang, X., and
1013   Chen, W.: Ozone control strategies for local formation- and regional transport-
1014   dominant scenarios in a manufacturing city in southern China, Sci. Total Environ., 813,
1015   10.1016/j.scitotenv.2021.151883, 2022.

1016   Mousavinezhad, S., Choi, Y., Pouyaei, A., Ghahremanloo, M., and Nelson, D. L.:
1017   A comprehensive investigation of surface ozone pollution in China, 2015–2019:
1018   Separating the contributions from meteorology and precursor emissions, Atmos. Res.,
1019   257, 10.1016/j.atmosres.2021.105599, 2021.

1020   Pan, X., Kanaya, Y., Tanimoto, H., Inomata, S., Wang, Z., Kudo, S., and Uno, I.:
1021   Examining the major contributors of ozone pollution in a rural area of the Yangtze
1022   River Delta region during harvest season, Atmos. Chem. Phys., 15, 6101–6111,
1023   10.5194/acp-15-6101-2015, 2015.

1024   Parrish, D. D., Ryerson, T. B., Mellqvist, J., Johansson, J., Fried, A., Richter, D.,

Walega, J. G., Washenfelder, R. A., de Gouw, J. A., Peischl, J., Aikin, K. C., McKeen, S. A., Frost, G. J., Fehsenfeld, F. C., and Herndon, S. C.: Primary and secondary sources of formaldehyde in urban atmospheres: Houston Texas region, Atmos. Chem. Phys., 12, 3273-3288, 10.5194/acp-12-3273-2012, 2012.

Sadanaga, Y., Kawasaki, S., Tanaka, Y., Kajii, Y., and Bandow, H.: New system for measuring the photochemical ozone production rate in the atmosphere, Environ. Sci. Technol., 51, 2871-2878, 10.1021/acs.est.6b04639, 2017.

Salthammer, T.: Acetaldehyde in the indoor environment, Environ. Sci. Atmos., 3, 474-493, 10.1039/D2EA00146B, 2023.

Shen, H., Liu, Y., Zhao, M., Li, J., Zhang, Y., Yang, J., Jiang, Y., Chen, T., Chen, M., Huang, X., Li, C., Guo, D., Sun, X., Xue, L., and Wang, W.: Significance of carbonyl compounds to photochemical ozone formation in a coastal city (Shantou) in eastern China, Sci. Total Environ., 764, 10.1016/j.scitotenv.2020.144031, 2021.

Shi, J., Bao, Y., Ren, L., Chen, Y., Bai, Z., and Han, X.: Mass concentration, source and health risk assessment of volatile organic compounds in nine cities of Northeast China, Int. J. Environ. Res. Public Health, 19, 4915, 10.3390/ijerph19084915, 2022.

Spaulding, R. S., Schade, G. W., Goldstein, A. H., and Charles, M. J.: Characterization of secondary atmospheric photooxidation products: Evidence for biogenic and anthropogenic sources, J. Geophys. Res., 108, 4247, 10.1029/2002JD002478, 2003.

Sillman, S.: The relation between ozone, NOx and hydrocarbons in urban and polluted rural environments, Atmos. Environ., 33, 1821-1845, 10.1016/S1352-2310(98)00345-8, 1999.

Sklaveniti, S., Locoge, N., Stevens, P. S., Wood, E., Kundu, S., and Dusanter, S.: Development of an instrument for direct ozone production rate measurements: measurement reliability and current limitations, Atmos. Meas. Tech., 11, 741-761, 10.5194/amt-11-741-2018, 2018.

Steinfeld, J. I.: Atmospheric chemistry and physics: from air pollution to climate change, Environ. Sci. Policy. Sustain. Dev., 40, 26-26,

1055   10.1080/00139157.1999.10544295, 1998.

1056   Tan, Z., Lu, K., Jiang, M., Su, R., Wang, H., Lou, S., Fu, Q., Zhai, C., Tan, Q.,
1057   Yue, D., Chen, D., Wang, Z., Xie, S., Zeng, L., and Zhang, Y.: Daytime atmospheric
1058   oxidation capacity in four Chinese megacities during the photochemically polluted
1059   season: a case study based on box model simulation, Atmos. Chem. Phys., 19, 3493-
1060   3513, 10.5194/acp-19-3493-2019, 2019.

1061   Tan, Z., Lu, K., Dong, H., Hu, M., Li, X., Liu, Y., Lu, S., Shao, M., Su, R., Wang,
1062   H., Wu, Y., Wahner, A., and Zhang, Y.: Explicit diagnosis of the local ozone production
1063   rate and the ozone-NOx-VOC sensitivities, Sci. Bull., 63(16):1067-1076,
1064   10.1016/j.scib.2018.07.001, 2018.

1065   Tan, Z., Fuchs, H., Lu, K., Hofzumahaus, A., Bohn, B., Broch, S., Dong, H.,
1066   Gomm, S., Häseler, R., He, L., Holland, F., Li, X., Liu, Y., Lu, S., Rohrer, F., Shao, M.,
1067   Wang, B., Wang, M., Wu, Y., Zeng, L., Zhang, Y., Wahner, A., and Zhang, Y.: Radical
1068   chemistry at a rural site (Wangdu) in the North China Plain: observation and model
1069   calculations of OH, HO_2 and RO_2 radicals, Atmos. Chem. Phys., 17, 663-690,
1070   10.5194/acp-17-663-2017, 2017.

1071   Tang, G., Zhu, X., Xin, J., Hu, B., Song, T., Sun, Y., Zhang, J., Wang, L., Cheng,
1072   M., Chao, N., Kong, L., Li, X., and Wang, Y.: Modelling study of boundary-layer ozone
1073   over northern China - Part I: Ozone budget in summer, Atmos. Res., 187, 128-137,
1074   10.1016/j.atmosres.2016.10.017, 2017.

1075   Wang, C., Yuan, B., Wu, C., Wang, S., Qi, J., Wang, B., Wang, Z., Hu, W., Chen,
1076   W., Ye, C., Wang, W., Sun, Y., Wang, C., Huang, S., Song, W., Wang, X., Yang, S.,
1077   Zhang, S., Xu, W., Ma, N., Zhang, Z., Jiang, B., Su, H., Cheng, Y., Wang, X., and Shao,
1078   M.: Measurements of higher alkanes using NO^+ chemical ionization in PTR-ToF-MS:
1079   important contributions of higher alkanes to secondary organic aerosols in China,
1080   Atmos. Chem. Phys., 20, 14123–14138, 10.5194/acp-20-14123- 2020, 2020.

1081   Wang, N., Lyu, X., Deng, X., Huang, X., Jiang, F., and Ding, A.: Aggravating O_3
1082   pollution due to NOx emission control in eastern China, Sci. Total Environ., 677, 732-
1083   744, 10.1016/j.scitotenv.2019.04.388, 2019.

1084   Wang, P., Chen, Y., Hu, J., Zhang, H., and Ying, Q.: Attribution of tropospheric
1085   ozone to NOx and VOC Emissions: considering ozone formation in the transition

regime, Environ. Sci. Technol., 53, 1404-1412, 10.1021/acs.est.8b05981, 2019.

Wang, Y., Zhang, Y., Hao, J., and Luo, M.: Seasonal and spatial variability of surface ozone over China: contributions from background and domestic pollution, Atmos. Chem. Phys., 11, 3511-3525, 10.5194/acp-11-3511-2011, 2011.

Wang, W., Parrish, D. D., Wang, S., Bao, F., Ni, R., Li, X., Yang, S., Wang, H., Cheng, Y., and Su, H.: Long-term trend of ozone pollution in China during 2014–2020: distinct seasonal and spatial characteristics and ozone sensitivity, Atmos. Chem. Phys., 22, 8935-8949, 10.5194/acp-22-8935-2022, 2022a.

Wang, W., Yuan, B., Peng, Y., Su, H., Cheng, Y., Yang, S., Wu, C., Qi, J., Bao, F., Huangfu, Y., Wang, C., Ye, C., Wang, Z., Wang, B., Wang, X., Song, W., Hu, W., Cheng, P., Zhu, M., Zheng, J., and Shao, M.: Direct observations indicate photodegradable oxygenated volatile organic compounds (OVOCs) as larger contributors to radicals and ozone production in the atmosphere, Atmos. Chem. Phys., 22, 4117-4128, 10.5194/acp-22-4117-2022, 2022b.

Wang, W.; Yuan, B.; Su, H.; Cheng, Y.; Qi, J.; Wang, S.; Song, W.; Wang, X.; Xue, C.; Ma, C.; Bao, F.; Wang, H.; Lou, S.; Shao, M.: A large role of missing volatile organic compound reactivity from anthropogenic emissions in ozone pollution regulation, Atmos. Chem. Phys., 24, (7), 4017-4027,10.5194/acp-24-4017-2024, 2024.

Wang, X., Zhang, T., Xiang, Y., Lv, L., Fan, G., and Ou, J.: Investigation of atmospheric ozone during summer and autumn in Guangdong Province with a lidar network, Sci. Total Environ., 751, 10.1016/j.scitotenv.2020.141740, 2021.

Wang, Y., Guo, H., Zou, S., Lyu, X., Ling, Z., Cheng, H., and Zeren, Y.: Surface O_3 photochemistry over the South China Sea: Application of a near-explicit chemical mechanism box model, Environ. Pollut., 234, 155-166, 10.1016/j.envpol.2017.11.001, 2018.

Whalley, L. K., Stone, D., Dunmore, R., Hamilton, J., Hopkins, J. R., Lee, J. D., Lewis, A. C., Williams, P., Kleffmann, J., Laufs, S., Woodward-Massey, R., and Heard, D. E.: Understanding in situ ozone production in the summertime through radical observations and modelling studies during the Clean air for London project (ClearfLo), Atmos. Chem. Phys., 18, 2547-2571, 10.5194/acp-18-2547-2018, 2018.

Whalley, L. K., Slater, E. J., Woodward-Massey, R., Ye, C., Lee, J. D., Squires, F., Hopkins, J. R., Dunmore, R. E., Shaw, M., Hamilton, J. F., Lewis, A. C., Mehra, A., Worrall, S. D., Bacak, A., Bannan, T. J., Coe, H., Percival, C. J., Ouyang, B., Jones, R. L., Crilley, L. R., Kramer, L. J., Bloss, W. J., Vu, T., Kotthaus, S., Grimmond, S., Sun, Y., Xu, W., Yue, S., Ren, L., Acton, W. J. F., Hewitt, C. N., Wang, X., Fu, P., and Heard, D. E.: Evaluating the sensitivity of radical chemistry and ozone formation to ambient VOCs and NOx in Beijing, Atmos. Chem. Phys., 21, 2125-2147, 10.5194/acp-21-2125-2021, 2021.

Wolfe, G. M., Marvin, M. R., Roberts, S. J., Travis, K. R., and Liao, J.: The Framework for 0-D Atmospheric Modeling (F0AM) v3.1, Geosci. Model. Dev., 9, 3309-3319, 10.5194/gmd-9-3309-2016, 2016.

World Meteorological Organization, Greenhouse Gas Bulletin No. 18, 2022, https://library.wmo.int/idurl/4/59137.

Wu, C., Wang, C., Wang, S., Wang, W., Yuan, B., Qi, J., Wang, B., Wang, H., Wang, C., Song, W., Wang, X., Hu, W., Lou, S., Ye, C., Peng, Y., Wang, Z., Huangfu, Y., Xie, Y., Zhu, M., Zheng, J., Wang, X., Jiang, B., Zhang, Z., and Shao, M.: Measurement report: Important contributions of oxygenated compounds to emissions and chemistry of volatile organic compounds in urban air, Atmos. Chem. Phys., 20, 14769–14785, 10.5194/acp-20-14769-2020, 2020.

Xue, L. K., Wang, T., Gao, J., Ding, A. J., Zhou, X. H., Blake, D. R., Wang, X. F., Saunders, S. M., Fan, S. J., Zuo, H. C., Zhang, Q. Z., and Wang, W. X.: Ground-level ozone in four Chinese cities: precursors, regional transport and heterogeneous processes, Atmos. Chem. Phys., 14, 13175-13188, 10.5194/acp-14-13175-2014, 2014.

Yang, S., Yuan, B., Peng, Y., Huang, S., Chen, W., Hu, W., Pei, C., Zhou, J., Parrish, D. D., Wang, W., He, X., Cheng, C., Li, X. B., Yang, X., Song, Y., Wang, H., Qi, J., Wang, B., Wang, C., Wang, C., Wang, Z., Li, T., Zheng, E., Wang, S., Wu, C., Cai, M., Ye, C., Song, W., Cheng, P., Chen, D., Wang, X., Zhang, Z., Wang, X., Zheng, J., and Shao, M.: The formation and mitigation of nitrate pollution: comparison between urban and suburban environments, Atmos. Chem. Phys., 22, 4539-4556, 10.5194/acp-22-4539-2022, 2022.

Yang, W., Chen, H., Wang, W., Wu, J., Li, J., Wang, Z., Zheng, J., and Chen, D.:

Modeling study of ozone source apportionment over the Pearl River Delta in 2015, Environ. Pollut., 253, 393-402, 10.1016/j.envpol.2019.06.091, 2019.

Yuan, B., Chen, W., Shao, M., Wang, M., Lu, S., Wang, B., Liu, Y., Chang, C.-C., and Wang, B.: Measurements of ambient hydrocarbons and carbonyls in the Pearl River Delta (PRD), China, Atmos. Res., 116, 93-104, 10.1016/j.atmosres.2012.03.006, 2012.

Yuan, B., Koss, A. R., Warneke, C., Coggon, M., Sekimoto, K., and de Gouw, J. A.: Proton-Transfer-Reaction Mass Spectrometry: applications in atmospheric sciences, Chem. Rev., 117, 13187–13229, 10.1021/acs.chemrev.7b00325, 2017.

Zhao, W., Tang, G., Yu, H., Yang, Y., Wang, Y., Wang, L., An, J., Gao, W., Hu, B., Cheng, M., An, X., Li, X., and Wang, Y.: Evolution of boundary layer ozone in Shijiazhuang, a suburban site on the North China Plain, J. Environ. Sci., 83, 152-160, 10.1016/j.jes.2019.02.016, 2019.

Zhang, X., Xu, J., Kang, S., Zhang, Q., and Sun, J.: Chemical characterization and sources of submicron aerosols in the northeastern Qinghai–Tibet Plateau: insights from high-resolution mass spectrometry, Atmos. Chem. Phys., 19, 7897-7911, 10.5194/acp-19-7897-2019, 2019.

Zhang, Y., Zhang, Y., Liu, Z., Bi, S., and Zheng, Y.: Analysis of vertical distribution changes and influencing factors of tropospheric ozone in China from 2005 to 2020 based on multi-source data, Int. J. Environ. Res. Public Health, 19, 10.3390/ijerph191912653, 2022.

Zhou, J.; Wang, W.; Wu, Y.; Zhang, C.; Liu, A.; Hao, Y.; Li, X.-B.; Shao, M.: Development and application of a nitrogen oxides analyzer based on the cavity attenuated phase shift technique, J. Environ. Sci., 150, 692-703, 10.1016/j.jes.2023.11.017, 2025.

Zhou, J., Yuan, B., Li, X., and Shao, M.: Measurement and modelling results of O_3 and its precursors [Data set]. Zenodo. 10.5281/zenodo.7854639, 2023.

Zhu, H., Wang, H., Jing, S., Wang, Y., Cheng, T., Tao, S., Lou, S., Qiao, L., Li, L., and Chen, J.: Characteristics and sources of atmospheric volatile organic compounds (VOCs) along the mid-lower Yangtze River in China, Atmos. Environ.,

1177   190, 232-240, 10.1016/j.atmosenv.2018.07.026 2018.

1178   Zhu, J., Wang, S., Wang, H., Jing, S., Lou, S., Saiz-Lopez, A., and Zhou, B.:
1179   Observationally constrained modeling of atmospheric oxidation capacity and
1180   photochemical reactivity in Shanghai, China, Atmos. Chem. Phys., 20, 1217-1232,
1181   10.5194/acp-20-1217-2020, 2020.

1182

1183

1184

1185